

Bifacial, thin-film (Ag,Cu)(In,Ga)Se₂ solar cells for tandem applications

Elizaveta Yakovleva Bengtson

November 2025

Abstract

This licentiate thesis summarises the common fabrication and characterisation techniques of (Ag,Cu)(In,Ga)Se₂ (ACIGS) solar cells. Important process steps and their effects on the properties of the solar cells are described, such as the multi-stage co-evaporation technique, Ga-grading of the absorber, and alkali treatment. Experimental results are presented with different characterisation methods to illustrate the effects of the process techniques. The role of ACIGS solar cells in the tandem solar cell structure is briefly discussed. The focus of the thesis is to show a cell fabrication process that yields good solar cell performance on the transparent back contact indium tin oxide (ITO). Studies of ACIGS on ITO are presented to show the benefits and challenges when working with this back contact compared to the standard, molybdenum back contact.



UPPSALA
UNIVERSITET

Contents

1.	Introduction	5
1.1.	CIGS solar cells	5
1.2.	Aim and brief outline of thesis	6
2.	Background	7
2.1.	Solar cell physics	7
2.1.1.	Loss mechanisms	9
2.2.	The chalcopyrite material	10
2.3.	CIGS Solar cell design	11
2.4.	CIGS deposition methods	13
2.5.	Bandgap-grading	14
2.6.	The three-stage process	15
2.7.	Silver-alloying	15
2.8.	Substrates and back contacts	16
2.9.	Transparent Conducting Oxides as alternative back contacts	16
2.10.	Passivation methods	17
2.11.	Alkali treatment	18
2.12.	Tandem solar cells	18
3.	Experimental methods	19
3.1.	Substrate preparation	19
3.2.	ACIGS deposition	21
3.3.	RbF treatment	23
3.4.	Buffer and window layers	23
3.5.	Cell definition and contacting	23
3.6.	Electrical and optical characterization	24
3.7.	Material characterization	25
4.	Research highlights	25
4.1.	Optimising the ACIGS process for ITO back contacts	26
4.2.	Comparing Mo and ITO back contacts	27
4.2.1.	Additional characterisation with CV and PL	29
4.3.	Ga-graded ACIGS on ITO	33
4.4.	Absorber thickness	34
4.5.	Importance of NaF precursor optimisation for ACIGS on ITO	36
4.6.	RbF PDT of ACIGS on ITO	37

4.7. Some comments about stability	40
5. Summary	41
6. Outlook	42
7. Acknowledgement	43
8. References	44
Appendix	49
9. Theory of characterization methods	49
9.1. Electrical and optical characterization	49
9.1.1. Current-voltage	49
9.1.2. External quantum efficiency	49
9.1.3. Capacitance-voltage	49
9.1.4. Photoluminescence	50
9.2. Material characterization	51
9.2.1. X-ray fluorescence spectroscopy	51
9.2.2. Mass spectrometry	52
9.2.3. Glow discharge optical emission spectroscopy	52
9.3. Electron microscopy	53
10. ACIGS deposition recipes	54
10.1. Cell processing post absorber deposition	54
10.2. Cell definition with photolithography	54
11. Optimisation of ACIGS process for ITO: additional figures	55
12. Deterioration of performance after dark storage	57
13. Manuscript	59

List of abbreviations

2T – Two-terminal
4T – Four-terminal
AC – Alternating current
ACIGS – (Ag,Cu)(In,Ga)Se₂
AZO – Aluminium-doped zinc oxide
CBD – Chemical bath deposition
CIGS – Cu(In,Ga)Se₂
CV – Capacitance-voltage
DC – Direct current
EDS/EDX - Energy dispersive X-ray spectroscopy
EQE – External quantum efficiency
GDOES – Glow discharge optical emission spectroscopy
GHG – Greenhouse gases
IR – Infrared
ITO – Tin-doped indium oxide (In₂O₃:Sn)
IV – Current-voltage
JV – Current density-voltage
LS – Light soaking
MS – Mass spectrometry
PCE – Power conversion efficiency
PDT – Post-deposition treatment
PL – Photoluminescence
PV – Photovoltaics
PVD – Physical vapour deposition
SCR – Space charge region
SLG – Soda-lime glass
STEM – Scanning transmission electron microscopy
TCO – Transparent conductive oxide
TEM – Transmission electron microscopy
TFSC – Thin film solar cell
XRF – X-ray fluorescence

1. Introduction

The global challenges of today's society are related to a rising demand on Earth's resources, and a climate that is becoming hotter and more unpredictable. The rising global temperature is a result of accumulated emissions of greenhouse gases (GHG) caused by human activities, such as burning fossil fuels, since the beginning of the industrialization. In 2011-2020 the surface temperature was 1.1°C above the 1850-1900 average, and the rate of global warming is only increasing [1]. One important effort in mitigating climate change is to transition to more sustainable energy sources and exchanging fossil fuels to renewable sources for the generation of electricity. Renewable energy is steadily gaining ground from coal, gas and oil. In 2028, renewable energy sources are expected to account for over 42% of global electricity generation, with more than half the share being from wind and solar photovoltaics (PV), as PV continues to provide a low-cost, available and scalable source of electricity [2]. The prospect for PV is that it has an important role in the global energy transition, and as long as continued progress is made with the technology, its cost-reduction, and deployment policies, the future scenario for PV looks bright [3].

Transitions from fossil-based electricity sources to PV technology can mitigate GHG emissions at a low cost. Despite its many benefits, PV technology can still affect the environment and human health. While metal depletion, land use and carcinogens are the main issues with PV technology, there is also an effect on climate change. Many of the impacts are related to the manufacturing of PV, which releases GHG and consumes water, and the connections with the electrical grid, which uses a lot of metals. Projected future development of module production and design, agrivoltaics and floating PV, as well as implementation of recycling, shows that these adverse effects will likely decrease [3], [4].

Today's PV market is dominated by Si solar cells, representing 98% of worldwide production [5]. Thin film solar cells (TFSCs) have the advantage over Si PV that they require less PV material, in the range of a few micrometres compared to hundred micrometres or more for Si. Compared to silicon solar cells, TFSCs also require less energy to be produced and release less GHG emission [6]. Still, Si holds market dominance due to the low module cost and high efficiency records that few TFSC materials can compete with [5]. The maturity and large scale of the Si industry is years ahead of other technologies, which explains the difference in price and performance. A probable future for TFSCs is therefore in multi-junction devices, also called tandem solar cells. The multi-junction architecture combines two (tandem) or more layers of PV material to use the solar spectrum more efficiently and achieve higher power output [7], [8], [9].

1.1. CIGS solar cells

Cu(In,Ga)Se₂ (CIGS) is a TFSC material which has proven to be an important contributor to the progress in PV, thanks to being highly absorbing, long-term stable, durable, and non-toxic [10]. The CIGS solar cells started out as p-type CuInSe₂ forming a pn-junction with a layer of n-type CdS. These devices had good absorption in the near infrared (IR) light spectrum. A later substitution of some of the In with Ga in the absorber increased the bandgap from 1.04 eV to 1.1-1.2 eV and increased the efficiency [10].

In recent years, several additions to the CIGS process have improved the material. Among those are addition of silver, treatment with alkali elements, and bandgap engineering with Ga-grading. Other parts of the solar cell have also been improved, such as the material of the window layer, the back contact, and the junction architecture. The addition of silver in exchange for some of the copper to form (Ag,Cu)(In,Ga)Se₂ (ACIGS) is beneficial for the opto-electronic properties since it lowers voltage losses and improves crystal grain size, especially at low temperature deposition [11], [12]. The latest world-record CIGS cells, which reached 23.64% efficiency, had a 20% silver to copper ratio and a bandgap-graded absorber profile [13].

By changing the composition of CIGS, the bandgap can be changed. A variation of the concentration of Ga to In, $[Ga]/([Ga]+[In])$ (GGI), changes the bandgap continuously between 1.0 eV and 1.65 eV [14]. This makes the material a good candidate for tandem solar cells, where the optimal bandgaps for light-absorption are 1.7 eV for a top cell and 1.1 eV for a bottom cell [15]. When the GGI is gradually increased towards the back of the solar cell, this is called a Ga-grading, and is used to reduce recombination at the back contact by lowering the minority carrier (electron) density [11]. Thereby the Ga-grading reduces the back contact recombination, since recombination is proportional to the product of electron and hole density.

Bifacial solar cells can generate electricity by absorbing light coming in both from the front and the rear surface of the device. Their increased yearly yield compared to monofacial PV, and the more versatile areas of application, such as vertically mounted modules and agrivoltaics, make bifacial PV a promising technology that is expected to dominate the PV market in the future [16]. The bifacial CIGS solar cells in this thesis use a transparent conducting oxide (TCO) instead of a metal back contact. So far, bifacial CIGS has not yet reached the same efficiency as monofacial CIGS, although recent progress has been made in improving the efficiency [17], [18].

1.2. Aim and brief outline of thesis

The goal of the PhD project is to fabricate a tandem solar cell with bifacial ACIGS as both top and bottom cells in the structure. This licentiate thesis focuses on the methods of depositing and characterizing the low-bandgap bifacial ACIGS solar cell that can be used as a tandem bottom cell. Applying the standard ACIGS deposition techniques on a transparent back contact was explored in a study, the results of which are presented and discussed in chapter 4. A study of RbF post-deposition treatment (PDT) of ACIGS is also presented in chapter 4. Before that, an introduction to ACIGS and its methods of fabrication are introduced in chapter 2. The experimental methods used in this thesis are summarized in chapter 3, while the theory behind the characterization techniques can be found for further reading in the Appendix, chapter 9. Chapters 5 and 6 provide a summary of the conclusions of the thesis and an outlook on future topics of interest.

2. Background

2.1. Solar cell physics

Solar cells convert photon energy to electrical energy. A basic model for the solar cell is a diode, which is formed by a p-type (acceptor doped) and an n-type (donor doped) semiconductor in direct contact. The junction between the n-type and p-type material is called the pn-junction. Carriers diffuse across the junction, electrons from the n-type region, and holes (positive charge or the absence of an electron) from the p-type region, leaving ionized atoms (positively charged in the n-type material and negatively charged in the p-type material) that induce an electrostatic field leading to a potential difference between the n-type and p-type side of the junction, counteracting further diffusion of holes and electrons. The potential difference is called the *built-in potential*. The transition region between the n-type and p-type material with the ions is called *space charge region* (SCR) or *depletion region*, because it is essentially depleted of free holes and electrons. On either side of the SCR region, there is almost no space charge, which is why these regions are called *quasi-neutral*. Figure 1 presents a schematic model of the pn-junction.

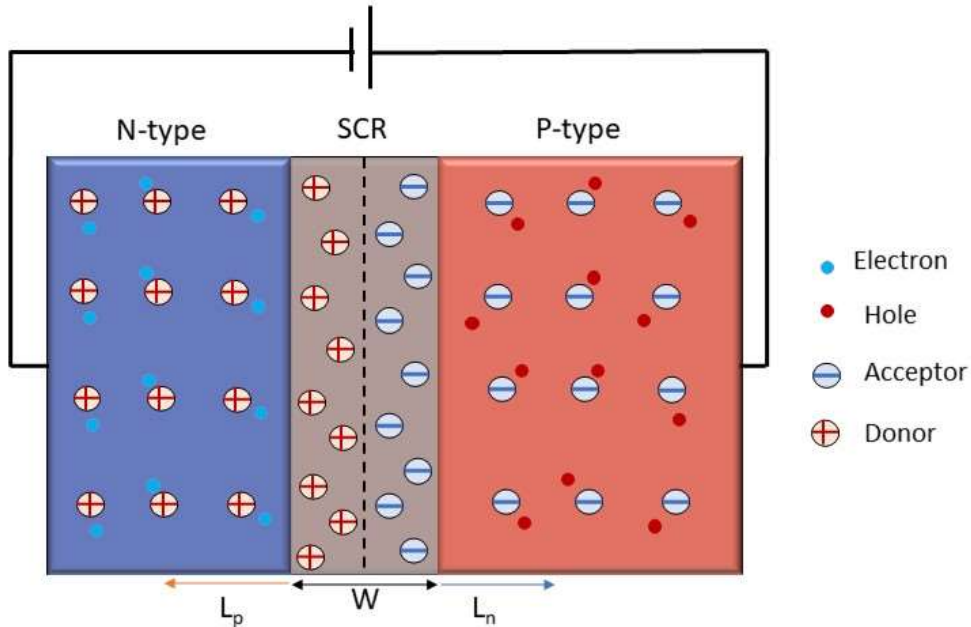


Figure 1 The pn-junction illustrated with a simple model. The SCR is marked out as the transition region between the n-type and p-type materials, with W being the width of the SCR, and the plus and minus signs signifying the dopant ions. The diffusion lengths, L_n for electrons in the p-type material and L_p for holes in the n-type material, are marked on their respective sides of the SCR. An external circuit with a forward bias can be connected to the ends of the pn-diode to extract the electrons at the n-side and inject them, after their energy has been used, on the p-side where they recombine with a hole.

Pairs of electrons and holes are generated throughout the pn-diode under illumination. The induced electrostatic field in the SCR sweeps any introduced negative electrical charges towards the n-type material (and holes towards the p-type material), which means that the charges are separated and less likely to recombine before they have been collected by an applied external potential. Minority charge carriers generated outside the SCR have a limited lifetime, determined by the minority carrier lifetime of the material at the n-type and p-type side, respectively, during which they can be collected before they recombine. Solar cells are operated under a forward bias, with an external

load connecting the front and rear of the solar cell, which allows carriers to be extracted from the solar cell, and their energy to be used by the external circuit, before being fed back to the solar cell.

The output characteristics of the solar cell are described by the current-voltage curve, where the short-circuit current density (J_{SC}), the open-circuit voltage (V_{OC}), and the fill factor (FF) can be extracted. The current density is used instead of current to more easily compare outputs of cells of different areas, since larger area means more photo-generated charge carriers. The ideal total photo-diode current, neglecting resistance losses and recombination, is given by the ideal diode equation:

$$J = J_0(e^{qV/kT} - 1) - J_L, \quad (1)$$

where J_0 is the dark saturation current, q is the elementary charge, V is the voltage across the external load, k is the Boltzmann constant, T is the temperature, and J_L is the light-generated current.

For the ideal solar cell J_{SC} is equal to the light-generated current,

$$J_{SC} = qG(L_n + W + L_p), \quad (2)$$

where G is the generation rate of charge carriers, W is the depletion width, L_n and L_p are the diffusion lengths of electrons and holes at the p-side (electrons) and n-side (holes), respectively. The generation rate depends on the photon flux at the surface, the absorption coefficient of the material (only photons with energy above the semiconductor bandgap contribute to the generation rate), and the distance from the surface of the material (generation decays exponentially in the bulk of the material). The diffusion length is the average distance that a carrier moves from point of generation to recombination, and is proportional to the square root of the carrier lifetime in the material. Equation (2) assumes collection of all carriers generated by light within a diffusion length of the diode's depletion region.

The relationship between V_{OC} and the current is found by setting $J=0$ in equation (1) above, and, assuming $J_L=J_{SC}$, the expression becomes

$$V_{OC} = \frac{kT}{q} \ln \left(\frac{J_{SC}}{J_0} + 1 \right). \quad (3)$$

The output of the solar cell is often summarized in one value, the power-conversion efficiency (PCE, η), given by

$$\eta = \frac{P_{out}}{P_{in}} = \frac{V_{OC} J_{SC} FF}{P_{in}}, \quad (4)$$

where the FF is the ratio between the V_{OC} , J_{SC} and the values of J and V at the maximum power (mp) point,

$$FF = \frac{V_{mp} J_{mp}}{V_{OC} J_{SC}}. \quad (5)$$

For cells of good efficiency, the FF value is normally in the range of 0.7-0.85, depending on the bandgap, recombination characteristics and parasitic resistances and/or electronic barriers in the solar cell.

The JV-curve of a well-performing ACIGS solar cell is shown in Figure 2. The performance characteristics J_{SC} , V_{OC} , J_{mp} , V_{mp} , and FF are marked out in the graph.

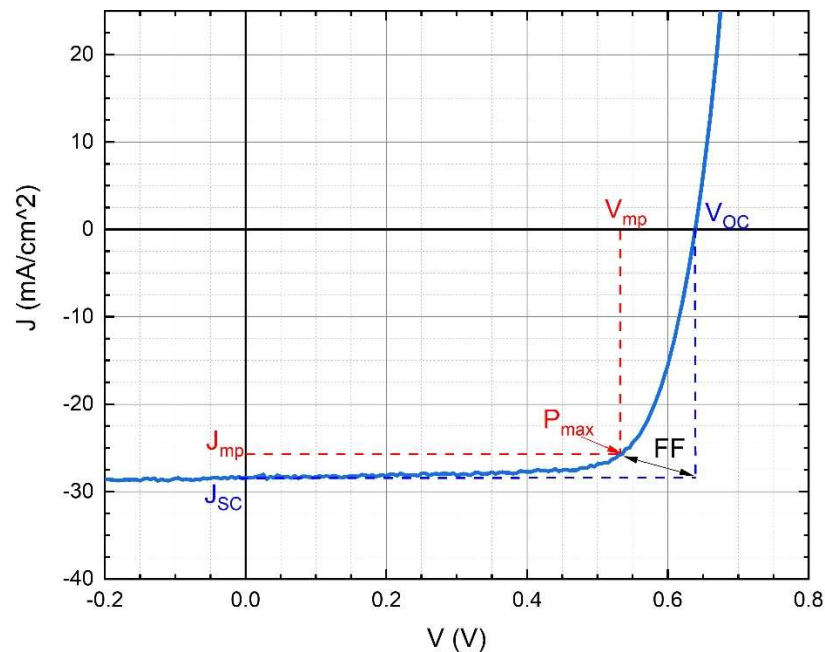


Figure 2 Typical JV-curve for an ACIGS solar cell measured under illuminated conditions. The V_{OC} and J_{SC} have been marked out where the curve crosses the voltage axis and current density axis, respectively. The V_{mp} and J_{mp} are the voltage and current density at the maximum power point (P_{max}), respectively. The FF is the ratio between these output characteristics and is an indication of how “square” the JV-curve is.

Because all performance parameters vary with temperature and the PV materials are sensitive to different wavelengths of the incoming light, performance measurements are always conducted at standard test conditions (STC). This means room temperature ($25^{\circ}C$), irradiance of 1000 W/m^2 (1 sun) and a spectrum that matches the solar spectrum from a clear sky at the sea level with the sun at an angle of about 42° above the horizon, known as the AM1.5 spectrum (the sunlight travels 1.5 times the distance through the atmosphere as compared to the sun being at the zenith angle).

2.1.1. Loss mechanisms

Different types of losses can occur in real solar cell devices that lower the performance compared to the ideal case. Solar cell design tries to minimise the losses and balance the trade-offs between losses of the different performance parameters.

Current losses are related to incomplete absorption of the incoming light or incomplete collection of the generated carriers. The former can be handled by decreasing external reflection, shading, parasitic absorption, or increasing the thickness of the light-absorbing layer. The latter losses are due to recombination of carriers, which is limited by passivating techniques, improved material quality and the bandgap gradients mentioned above.

Open circuit voltage losses are related to recombination in the solar cell. FF losses are mainly due to recombination in the SCR and parasitic series and shunt resistance losses. V_{OC} and FF losses

can be limited by increasing the quality of the material to limit the parasitic resistances and recombinations through defects, and passivation to limit recombination at interfaces.

A phenomenon that is often discussed in relation to V_{OC} loss is tail states. Tail states are energy states within the bandgap, which although forbidden in the ideal case, do occur in real devices. The distribution of tail states depends on structural defects/deviations, grain boundaries, electrostatic fluctuations due to doping compensation, and is often seen to follow an exponential decay, characterized by the Urbach energy, with a higher Urbach energy meaning more tail states. The Urbach energy is estimated from the absorption edge in the EQE. Thereby, it will also be influenced by other factors, such as bandgap grading and incomplete absorption, which makes its evaluation sometimes difficult, especially in thin, graded films. Rb treatments, higher process temperature and addition of Ag have been observed to lower the Urbach energy [14], [19].

2.2. The chalcopyrite material

(A)CIGS is a chalcopyrite material, meaning its lattice is formed of the I-III-VI₂ compound in a tetragonal crystal structure. ACIGS solar cells can be made in the same way as CIGS solar cells and have similar properties. However, in several instances ACIGS has shown a different behaviour compared to CIGS made with the same fabrication method. For instance, ACIGS has reduced net doping density and reacts differently to light and heavy alkali treatment [11], [20], [21]. The addition of Ag is relatively new and not all CIGS research groups have adopted it in their deposition methods, therefore all the effects of Ag on the CIGS material might not yet be fully known or understood. Yet the silver-alloying has already proven its relevancy as the current world-record chalcopyrite solar cell has an ACIGS absorber grown with a Ga-grading towards the back contact, with Rb added in a PDT, and light soaking (LS) used to achieve maximum efficiency [13].

Ag-alloying improves the efficiency of CIGS by increasing V_{OC} . Ag lowers the melting temperature of the chalcopyrite material, which improves crystal quality at lower deposition temperatures [11], [22]. The drawback of using Ag is its higher price compared to Cu, as well as metastabilities that have been reported in relation to LS of ACIGS devices, although some beneficial effects of the LS could also be seen [23]. At high Ag-concentration (20% Ag to Cu ratio) and high Ga-concentration (GGI~0.75) these metastabilities have reportedly caused device degradation [20].

As mentioned in the introduction, varying the composition of CIGS changes its properties. The bandgap can be engineered through addition of Ga in exchange for In, which raises the conduction band minimum (CBM), or addition of Ag in exchange of Cu, which mainly lowers the valence band maximum (VBM) [22]. Both Ga and Ag widen the bandgap, but the bandgap increase with Ga addition is higher. The chalcopyrite can also be grown as a sulphide, by exchanging some or all of the Se with S, which further widens the bandgap and can increase it to 2.4 eV for CuGaS₂ [24]. Theoretically, all compositions have similar maximum efficiencies [24], however fundamental differences between the wide-gap material and CIGS with low Ga-content lead to deposition of high-efficiency wide-gap CIGS being difficult to achieve with the same methods as low-bandgap CIGS. The highest efficiency for the chalcopyrite material has been reached with (Ag,Cu)(In,Ga)Se₂ with a minimum bandgap of 1.15 eV and a composition with $[Ag]/([Ag]+[Cu])$ (AAC) close to 0.2, GGI close to 0.3 and slightly off-stoichiometric with $([Ag]+[Cu])/([Ga]+[In])$ (I/III) at 0.84 [13].

The bandgap of any $(\text{Ag}_w\text{Cu}_{1-w})_z(\text{In}_{1-x}\text{Ga}_x)\text{Se}_2$ alloy composition can be determined with the proposed empirical formula [22]

$$E_g(eV) = 0.18w + 0.16w^2 + 4.44z - 2.63z^2 + 0.42x + 0.11x^2 - 0.22wx - 0.11wz + 0.24zx - 0.87 \quad (6)$$

Here x is the GGI ratio, w is the AAC ratio, and z is the I/III ratio. Other empirical formulas have also been proposed to model the dependence of the bandgap on the composition.

Increasing the GGI from 0 to 1 linearly increases the bandgap of CIGS from 1.0 eV to 1.7 eV. The open circuit voltage, V_{OC} , is expected to increase linearly with the bandgap and the current density is expected to decrease, since the absorption decreases, due to a lower number of photons with energy above the bandgap. However, devices with bandgaps above 1.3 eV have shown a V_{OC} (and FF) loss, leading to a non-linear increase in V_{OC} with the bandgap and an overall decline of efficiency [24], [25]. The voltage loss from increased Ga-content is believed to be related to an increase in shallow defects, leading to increased recombination [24], in addition to other interface and bulk properties that differ from the chalcopyrite material with low Ga-content, such as the band alignment with the CdS buffer layer.

Addition of alkali elements to the chalcopyrite material has been proven important for performance [14]. Na treatment was discovered first and by serendipity, because soda-lime glass (SLG) substrates were used, which contain Na that can diffuse into the absorber. It was later shown that heavier alkalis in addition to Na, such as K and Rb, added through a PDT further improves cell performance by improving V_{OC} and FF [13], [14], [26]. Alkali treatment will be discussed in chapter 2.11 of this thesis.

2.3. CIGS Solar cell design

The standard CIGS solar cell stack is made in the substrate configuration and has looked the same since the 1990's [27]. The stack from bottom to top consists of a substrate (usually soda lime glass (SLG)) for mechanical stability, Mo back contact, (A)CIGS absorber, CdS buffer layer to create the pn-junction, high-resistance ZnO, Al-doped ZnO (AZO) top contact, and, for improved collection, an Al or Ni grid. Figure 3 shows a schematic image (not to scale) of the (A)CIGS solar cell stack, with the common thicknesses of the layers included, and a scanning transmission electron microscopy (STEM) image of a cross-section of an incomplete ACIGS solar cell stack without the AZO and metallic grid.

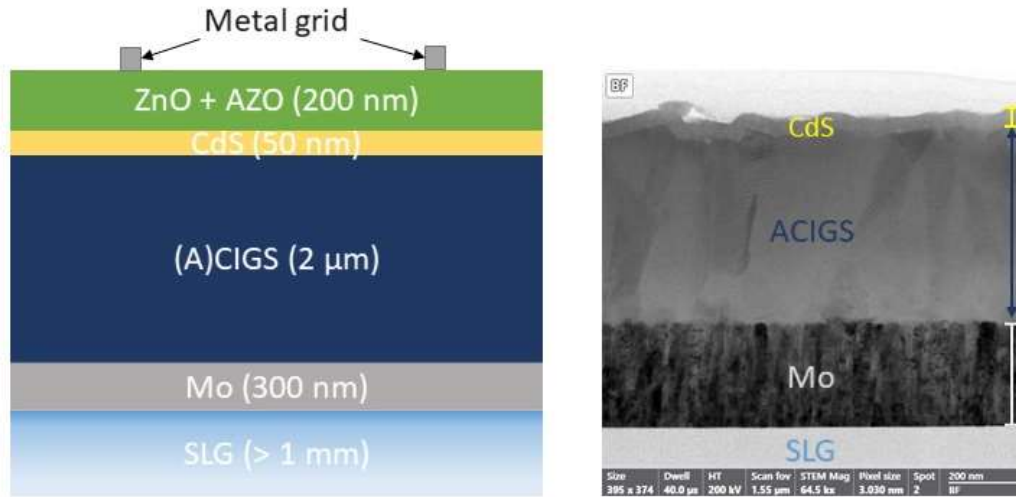


Figure 3 The (A)CIGS solar cell stack with common materials and thicknesses of the layers in a schematic figure on the left. On the right is a STEM bright-field (BF) image of a cross section of a SLG/Mo/ACIGS/CdS stack with a ~650 nm ACIGS layer.

Mo has good conductivity for collecting the current at the back of the cell. The metallic surface also reflects part of the light that was not absorbed on its first way through the absorber, thus increasing the probability of absorption [28]. MoSe₂ forms at the interface between Mo and CIGS, creating an ohmic contact [29]. Due to its alignment with the CBM and VBM of low- to mid-bandgap CIGS solar cells the MoSe₂ can create a weak back surface field to reduce recombination at the back contact. However, the recombination velocity, S_b , at the Mo back contact is still considered to be high, close to the thermal velocity of the charge carriers.

The CdS buffer layer is made thin (30-70 nm). CdS has a bandgap of 2.4 eV and thinning down of the CdS limits the parasitic absorption of blue photons. The pn-junction formed by the CIGS and CdS layers creates the electric field that separates generated charge carriers [28]. The CdS buffer is not ideal for wide-bandgap CIGS, because it creates a cliff in the energy bands at the CIGS/CdS interface, which can act as a recombination centre [24]. While the interface between low-bandgap CIGS and CdS is beneficial, there are other reasons to move away from the CdS buffer, such as the previously mentioned parasitic absorption of short-wavelength photons and the toxicity of Cd [30], [31].

On top of the CdS buffer, a TCO is used as a front contact and window layer. A high transmittance is necessary to maximize the absorption in the active part in the solar cell. Different TCOs exist, but the choice for chalcopyrite cells is limited by the requirements of low resistivity, high transparency in the range from ultraviolet (UV) to near infrared (IR), and a low deposition temperature (below 200°C). A common choice for the window layer is therefore a high-resistive ZnO (with no intentional doping) on top of the CdS, followed by an Al-doped ZnO (AZO) layer. The AZO provides the lateral conductivity on top of the device, while the undoped ZnO layer is introduced to avoid some negative electrical effects, such as shunts, that can form between the buffer and window layer [30]. To get the highest lab cell efficiencies it is also possible to add a layer of MgF₂ (approximately 100 nm thick) on top of the TCO as an anti-reflective coating to minimize optical losses [10], however this is not necessary for modules as their encapsulation provides a good refractive index matching that of air, which reduces reflectance.

Several strategies have been explored and adopted to improve the performance and production throughput of CIGS solar cells. The main strategies include lowering the absorber thickness [32], using transparent or flexible substrates [17], [33], bandgap-grading [34], passivation and light-management methods [35], [36], and alkali treatment [26], [37].

Thinner absorbers increase production throughput and use less critical raw material. However, problems with light-absorption and recombination at the back contact make implementation of passivation and light-management strategies especially important [35].

2.4. CIGS deposition methods

The two common techniques for depositing CIGS are physical vapor deposition (PVD), such as co-evaporation, and sputtering from precursors followed by a selenization step [10], respectively. With co-evaporation, the separate elemental sources are heated to temperatures in the order of 1000°C (except Se, which is only heated to several 100°C) and their evaporation rates controlled individually. The substrate is also heated, commonly to a maximum temperature of 550°C. In the lab setup employed for this thesis work, the evaporation flux of the elements is monitored *in situ* with mass spectrometry and the information is fed back to the temperature control of the sources. The possibility of careful control of individual elemental rates, substrate temperature, and film thickness makes this technique flexible and successful in producing high-efficiency, reproducible solar cells. The challenge with this technique lies in the control of the evaporation rates, requiring good and stable rate monitoring and control.

Deposition from precursors can be done with sputtering, but alternatives, such as electrodeposition or other processes have also been employed. The sputter precursor targets usually contain Cu, In and Ga of a certain elemental ratio, and the targets can be completely mixed (also with Se), or partially mixed (Cu-Ga and In) and used in sequence. The precursors are deposited on the substrate before being selenized (and/or sulfurized) through annealing in a Se-containing vapour. The precursors determine the metal composition of the film. The selenization can be done in a H₂Se (or H₂S for addition of S) environment, where the film is annealed at 400-500°C. H₂Se and H₂S are hazardous gases, and they can cause adhesion problems, but with careful process and environment control these challenges can be solved. The sputtering technique can easily be scaled up and sputtering of the precursors can be quick, which is important for high manufacturing throughput. Selenization post-treatment can take hours, which is why some manufacturers use hybrid processes, such as sputtering precursors that already contain Se [38].

The standard film is grown somewhat group-I-poor, with I/III~0.85-0.95, because this has yielded the best solar cell performance [34]. A phase with over-stoichiometric Cu and Ag can be used to enhance grain growth, but if the final composition of the films is too close to stoichiometry (1:1:2), or over stoichiometric (1⁺:1:2) they risk forming shunt-conductive secondary phases, such as Cu₂Se.

After absorber deposition, the buffer layer needs to be deposited quickly before the CIGS film oxidizes. The common CdS buffer layer is deposited in chemical bath deposition (CBD), which is a wet process. Alternative buffer layers that have been proposed are either deposited with CBD or in atomic layer deposition (ALD). The window layer is deposited at a maximum of 200°C to avoid

damaging the rest of the solar cell stack. The undoped ZnO and AZO are sputtered on top of the CdS [30].

Individual cells are defined with mechanical scribing or a technique called photolithography. Thin-film modules are scribed during the deposition process, forming monolithically interconnected cells. This is an advantage over Si modules where individual cells are interconnected after the cell processing steps, adding the extra steps of sorting cells and adding interconnections.

Front metal contacts can be added by evaporation through a shadow mask or with photolithography. Metal contacts improve the lateral conductivity and allow the window layer to be more transparent rather than conducting, decreasing parasitic absorption, although the contacts themselves add shading losses.

2.5. Bandgap-grading

Varying the GGI changes the band-gap of CIGS since Ga increases the CBM. The GGI can be continuously varied throughout the CIGS film by changing the rate of Ga and In during co-evaporation or using targets of different composition at different stages of a sputtering deposition. The resulting Ga-grading in the film is directly related to the bandgap grading, which is illustrated by equation (6) for bandgap calculation, where changing x (GGI) will change the bandgap, E_g .

The Ga-grading can be of different designs. In the world record device, [13] a ‘hockey stick’-like back-surface gradient was used. Earlier works have used grading at the front and back, so called double grading, with a notch at the lowest GGI value [33], [39]. Double Ga-grading leads to reduced recombination both at the front and back, which can promote charge carrier collection. However, the front gradient has been shown to decrease the FF and introduce a barrier when it is too steep or too wide. The Ga-grading also influences the absorption of light, since it changes the bandgap of the absorber, which can lead to absorption losses.

An article by Lundberg et al. [34] from 2004 discusses the importance of Ga-grading at the back contact, especially for thin absorbers. When the GGI varies throughout the bulk, the increase in bandgap reduces the carrier density, which can be modelled as inducing an electric field which repels electrons. For standard devices (1-2 μm thickness) the device improvement from Ga-grading is mostly in J_{SC} from better carrier collection thanks to the additional electric field, but in thin devices, the higher bandgap near the back contact can lead to loss of current due to lower near IR light absorption. For thinner devices the grading improves V_{OC} and FF by passivating the back surface. Lundberg et al. found no evidence of the need for a high GGI at front, which is otherwise characteristic of the notch profile.

Ga-grading can be created in a three-stage process (described below) where Ga and In are not evaporated during part of the deposition, which can lead to a natural or enhanced double grading [33], [34], [39]. It can also be created through the addition of Ga at the early or late stage of the deposition, since Ga does not diffuse easily in the CIGS material [11], [28], [40].

2.6. The three-stage process

The three-stage process was developed to fabricate high-efficiency CIGS solar cells with a graded bandgap in a PVD co-evaporation process [27]. This method of film growth creates films with large grains and a notch profile. The three stages are:

1. Cu-free stage. Substrate is at a lower temperature (300-450°C). Se, In and Ga are evaporated.
2. Cu-rich (In and Ga-free) stage. The substrate temperature is elevated to the maximum ($\geq 550^\circ\text{C}$). Se and Cu (and Ag) are evaporated until the film becomes slightly Cu-rich.
3. Cu-free stage. The substrate temperature is kept at the maximum. Se, In and Ga are evaporated without Cu (and Ag) once again.

After the third stage, the film is cooled down in the remaining Se vapor (for selenization) and then in vacuum. Se is provided throughout the deposition at a constant or variable rate which is always higher than the combined rate of the other elements. The ratio between the Ga and In depends on which bandgap the finished film should have. The Cu (Ag) diffuses in the film during the process, thus the group-I profile becomes flat. The movement of Cu ions happens in exchange for Ga and In ions, where In is more likely to diffuse, which is what creates the Ga-grading in the final film [40].

There exist different versions of the three-stage process, also called multi-stage process. One option is to provide all elements in all three stages, but that the film is still grown group-I-poor in the first and third stages. The group-III elements can also be varied in two stages instead of three, with the first stage having high GGI and the second having low GGI to have more control over the grading and confine the grading to the back contact [11]. This process was used in this thesis.

The success of the three-stage process is attributed to the large crystal grains formed during growth, as well as the formation of the Ga-grading. While record solar cells have been made with this process, it is not so common in industry due to the need for multiple elemental sources and usually longer deposition time [41]. More common in industrial manufacturing is to have an in-line process, where the substrate moves past stationary sources during deposition.

2.7. Silver-alloying

Ag can be incorporated into CIGS through a precursor layer [19] or co-evaporation simultaneously with the other sources [11]. The former is a method that allows ACIGS to be grown in pre-existing CIGS co-evaporators without installing an additional Ag-source, while the latter method often allows precise control of the Ag evaporation rate throughout the deposition.

By combining Ag and Ga incorporation, a wider bandgap, and thus a higher voltage, can be achieved with lower Ga-content [11]. Ag also allows the deposition temperature to be lowered. A study by Yang et al. [19] demonstrated how ACIGS cells could be deposited at a substrate temperature as low as 303°C without significant loss of efficiency. The main finding was that ACIGS deposited at low temperatures still yielded large, uniform crystal grains and high V_{OC} , unlike CIGS which displayed significant V_{OC} loss, low Cu diffusion, and small grains at temperatures below 450°C . Lower deposition temperature is beneficial as it can lower manufacturing costs, decrease thermal stress [19], promote formation of compositional profiles (this

effect is further enhanced by the Ag itself) [12], maintain the quality of TCO back contacts and allow deposition on polyamide substrates [17], [33].

Ag even improves crystallinity in high-Ga regions, which is important for graded and wide-bandgap solar cells, where it can help overcome the voltage deficit. The benefits of ACIGS can in part be explained by the lower density of structural defects, seen by measuring a lower Urbach energy compared to CIGS [19].

2.8. Substrates and back contacts

CIGS solar cells are typically made with Mo back contacts on SLG substrates. The Mo is usually sputtered onto the glass, making sure the metal film has good conductivity for current collection at the back contact. SLG is used because of its availability, durability, flat surface and a thermal expansion coefficient that works well with CIGS. The SLG is also a source of Na, and in some cases of K, which can diffuse through the Mo into the CIGS, providing a source, although not a controllable one, of the beneficial alkali elements. Both Mo and SLG can handle the high deposition temperatures normally used for CIGS [10].

There can be situations where other substrates and back contacts are preferable, even though they come with their own challenges. Glass is heavy and rigid, while steel and polyimide can be flexible and lightweight. Lightweight substrates are of interest for space and vehicle PV applications. In semi-transparent or bifacial applications, Mo has to be exchanged for a TCO, which provides transparency at the loss of some conductivity. In this thesis Mo back contacts have been used as a reference, while the objective has been to demonstrate ITO as a good, transparent alternative.

2.9. Transparent Conducting Oxides as alternative back contacts

TCOs belong to a group of materials that are both conductive and transparent. The commonly used TCOs are n-type and highly doped [42], since an un-doped oxide is usually an insulating material. The increased conductivity from the doping increases the absorption of light, especially in the IR, which is the main trade-off with TCOs. TCOs are used in the window layers of all thin film solar cells and some Si-based cells and as transparent back contacts in bifacial solar cells [10].

A number of TCOs have been tested as transparent back contacts (TBCs) for CIGS. These include fluorine-doped SnO_2 (FTO), tin-doped In_2O_3 (ITO), hydrogen-doped In_2O_3 (IOH), tungsten-doped In_2O_3 (IWO), and aluminium-doped ZnO (AZO). The main problem with TCOs as TBCs is an observed FF loss when comparing to cells made on the standard Mo contact [43]. The reasons for this FF loss have not been completely understood. The listed TCOs are n-type material, which could imply that an unfavourable Schottky-diode (reverse pn-junction) should form at the TCO/CIGS interface, and yet the TCO/CIGS interface has reportedly provided a good ohmic contact [44]. The FF loss has also been related to GaO_x formation during high-temperature growth of CIGS [17], [43]. GaO_x is a highly resistive, high-bandgap material that can create a barrier for holes when it is formed in the TCO/CIGS interface. The formation of GaO_x can also lead to a reduction in the GGI, which can cause a reversed Ga-grading. Effort has been put into limiting the GaO_x formation, which is catalysed by high temperature and Na content [17], [18], [43], [45].

The different TCOs have individual strengths and challenges. CIGS on FTO does not grow a GaO_x layer [46]. However, FTO loses conductivity at high temperatures [46] and has lower optical transmission compared to AZO, IWO and IOH [42]. ITO at low sheet resistances has high absorption in the IR. From an optical point of view, IOH and IWO are the best for (A)CIGS, because of their stable transmittance at longer wavelengths, low absorption of IR light, and high electron mobility. Electronically, however, ITO has shown superior performance, retaining its conductivity after heating and when kept in a humid environment [42], [43]. Therefore, ITO is often the more promising choice for TBC for solar cells, although with this choice lower deposition temperatures, which can lower absorber quality, are still required to limit the GaO_x growth [18]. For high bifaciality, alternative solutions to ITO are needed. However, because of its electronically superior performance with no electronic barriers and sufficient conductivity for cells, ITO was the material of choice for the work in this thesis.

2.10. Passivation methods

Passivation methods are used to decrease recombination. As discussed previously, recombination leads to voltage losses and current losses. Therefore, passivation has become very important in several PV fields to reach the highest efficiencies.

Interfaces and grain boundaries are areas in the solar cell that are particularly prone to cause recombination losses due to the usually large number of loose bonds or unoccupied bandgap states occurring where the crystal structure is altered. Surfaces can be passivated by adding a material, such as SiO_x or Al_2O_3 , which improves the electronic structure by introducing a field effect from fixed negative charges [47]. A different passivation approach is increasing the local doping at the interface or a contact, which introduces a back-surface field (BSF). The effect of the BSF is a weak barrier for minority carriers, meaning the relative minority carrier density decreases at the surface relative to the bulk, lowering the recombination of minority carriers at the surface [10]. A too high doping may, however lead to increased recombination of minority carriers by defect-related or Auger recombination, which lowers the voltage, therefore the volume with the increased doping needs to be limited, mainly to contact areas, for example to the back contact in thin solar cells.

Passivation becomes especially important when the high-recombination region is within a diffusion length of the SCR, because this will increase the number of carriers reaching the area and recombining. The front surface and the bulk are therefore important to passivate, because the SCR is usually close to the front where most carriers are generated. If the absorber is thick, the SCR is far from the rear surface, which then has little effect on carrier collection. The thinner the absorber becomes, the closer the SCR moves towards the rear interface, and the more influence this interface will have on carrier collection. Thus, to make thin solar cells, rear surface passivation techniques become essential to reach high current and voltage.

For CIGS, an important passivation technique for grain boundaries and the front surface is the alkali treatment [48]. Bandgap grading and Al_2O_3 and SiO_2 local structures have been used to passivate the rear surface [32], [49], [50]. These techniques allowed the reduction of absorber thickness in the lab and in an in-line process to $\leq 1 \mu\text{m}$, which had previously resulted in large voltage and efficiency losses.

2.11. Alkali treatment

The introduction of alkali treatment of the CIGS material led to great improvements in cell performance, increasing V_{OC} and FF. The introduction of Na proved important for dopant density, grain growth, grain boundaries and surfaces [10], [14], [51], and later treatments with the heavier alkalis K, Rb, or Cs improved voltage through interface passivation [26]. Na can be incorporated from the SLG or added after back contact deposition, for example as a NaF precursor layer [51], in a PDT or co-evaporated in the CIGS co-evaporation process [37]. Certain materials (such as SiO_x , Al_2O_3 , IOH, and ITO) can block the Na diffusion from the SLG to the CIGS [10], [43]. In those cases, and when the substrate does not contain Na (such is the case for steel and polyimide), Na needs to be actively provided to the CIGS during deposition. Similarly for the case of K, which can come from potassium-rich glass, but is often provided post-deposition [11]. Rb or Cs are usually added through PDT. When the fluoride-alkali compound reacts with the CIGS material, the F is only somewhat incorporated, but most of it is evaporated or flushed away in the subsequent CdS CBD, and what remains is the alkali incorporated in the CIGS lattice [37], [52].

PDT with heavy alkali also improves V_{OC} by decreasing bulk recombination. Several origins for the improvement have been debated. A proposed explanation of the alkali effect is that the recombination in the bulk and at the grain boundaries is reduced, thanks to a decreased density of electronic tail states because of upward band bending at the grain boundaries [14], [26]. The effect likely originates at the grain boundaries because this is where the heavy (and light) alkali elements accumulate and form compounds with wider bandgap than the bulk CIGS [37]. The PDT also alters the surface composition of CIGS, passivating the surface [14].

An important benefit of the heavy alkali PDT is the possibility to reduce the thickness of the CdS buffer layer without losing V_{OC} . The thinner buffer has less parasitic absorption, which increases the J_{SC} of the device [14].

If no Na is provided, this is detrimental for device performance, but too much Na also deteriorates performance and decreases adhesion between the absorber and the back contact [53]. The NaF layer is gradually consumed during the growth process, and if there is a lot of NaF remaining during the CdS CBD (or any water containing) process, the water-soluble NaF will lead to peel-off of the CIGS from the back contact. Similar adhesion issues with thick Na-containing Mo layers (MONA) have been reported [54]. It has been observed that ACIGS has a lower optimum amount of added NaF and KF compared to CIGS [11], [43].

Exposing the solar cells to continuous illumination for a longer period of time, LS, is used by most groups to achieve the best performance of CIGS solar cells. The LS treatment is particularly important to unlock the benefits of alkali treatment [13], [55].

2.12. Tandem solar cells

Tandem solar cells were introduced as a way to use the solar cell spectrum more efficiently than a single solar cell, which has a 30% theoretical efficiency limit, as predicted by Shockley and Quiesser [7]. By adding another absorbing layer to the solar cell stack, the bottom absorber is illuminated

with only a fraction of the light spectrum, yet the theoretical maximum efficiency of the two cells is increased to 42%. By adding more layers, the tandem structure can reach up to 68% efficiency (or 86% with light-concentration) [8]. In practice, the efficiencies will be lower than the theoretical maximum, especially since each added layer adds complexity to the design, and careful matching of absorber bandgaps is necessary [9]. The tandem device can be constructed in different ways, with two main examples being the monolithic two-terminal (2T), with one cell grown on top of the other, and the four-terminal (4T), where the two cells are separate devices.

CIGS has good potential for tandem solar cell applications, thanks to the possibility to tune the bandgap in the range 1.0-1.7 eV (or up to 2.4 eV with S instead of Se). It is therefore possible to make a tandem with CIGS as both top and bottom cell. However, in addition to the technical difficulties of making a tandem cell, the CIGS-buffer interface is temperature sensitive and can be damaged from the growth of another CIGS layer on top of it. Thus, a 4T structure might be easier to synthesize. Recent results have shown that lower bandgap (around 1.11-1.15 eV) ACIGS can now be achieved with high efficiency [13], ensuring that the bottom cell functions at high efficiency. The major remaining challenge is making a high-efficiency, wide-gap (A)CIGS top cell. Here, recent results suggest that sulfur-based ACIGSu may be a possible way forward [56].

Another potential tandem structure is CIGS with a perovskite top cell. Perovskite/CIGS tandem solar cells have been synthesized, with the latest published 2T result of 28% power conversion efficiency [57]. The challenge with this design is the low stability of the perovskite material [58]. Both 4T and 2T tandem with CIGS have been suggested. In a 2T tandem structure it is useful to have a bifacial cell to allow rear illumination and thus balance the current generation between the low and high bandgap cells [17]. If the perovskite stability and the current matching in a 2T tandem can be solved, this type of cell holds potential for high-performance modules in the future.

3. Experimental methods

Before going into the research results, it is appropriate to describe how the solar cell samples were prepared and characterized in the Solar Cell Technology lab at the Ångström laboratory, Uppsala University. Detailed recipes for the processes can be found in the Appendix.

3.1. Substrate preparation

The substrates used in the experiments were SLG with Mo or ITO for back contacts. The Mo substrates were all of the same type, with 300 nm sputtered Mo on 3 mm standard SLG. Several ITO substrates were tested in the experiments: 1.1 mm SLG with 350 nm ITO from MSE PRO, 375 nm ITO on 2 mm SLG from Saint-Gobain, and ~400 nm ITO deposited in-house on 2 mm SLG. The in-house ITO was deposited using DC magnetron sputtering in the von Ardenne, model CS730. Some ITO samples were annealed in vacuum before ACIGS deposition to increase transparency and conductivity. Table 1 lists the substrate types with sheet resistances and transmittance at a wavelength close to the bandgap of the ACIGS absorbers investigated as part of this thesis (around 1.11 eV).

Table 1: Properties of the substrates used in the experiments of this thesis. The annealed ITO-3 substrates had sheet resistance 35-37 Ohm/Sq before annealing in a vacuum environment. The transmittance is given as a percentage at the wavelength close to the bandgap edge of the ACIGS absorbers deposited for this thesis.

Back contact	Glass thickness [mm]	Material thickness [nm]	Sheet resistivity [Ohm/Sq]	Transmittance (at 1100 nm) [%]
Mo	3	300	0.5	0
ITO-1	1.1	350	3-5	41
ITO-2	2	375	6	54
ITO-3 (as-deposited)	2	380	40-50	75
ITO-3 (annealed)	2	390	16-18	84

The transmittance and reflectance of the different ITO substrates used for ACIGS deposition as part of this thesis are presented in Figure 4 Transmittance (T, solid lines) and reflectance (R, dashed lines) as a function of wavelength for four different ITO substrates used for ACIGS deposition in this thesis.. The transmittance and reflectance measurements were performed on untreated substrates, and these properties, along with the conductivity, are known to change during annealing and ACIGS growth. Despite a likely change in properties after ACIGS deposition, this graph gives an indication of the optical properties of the substrates and the differences between them.

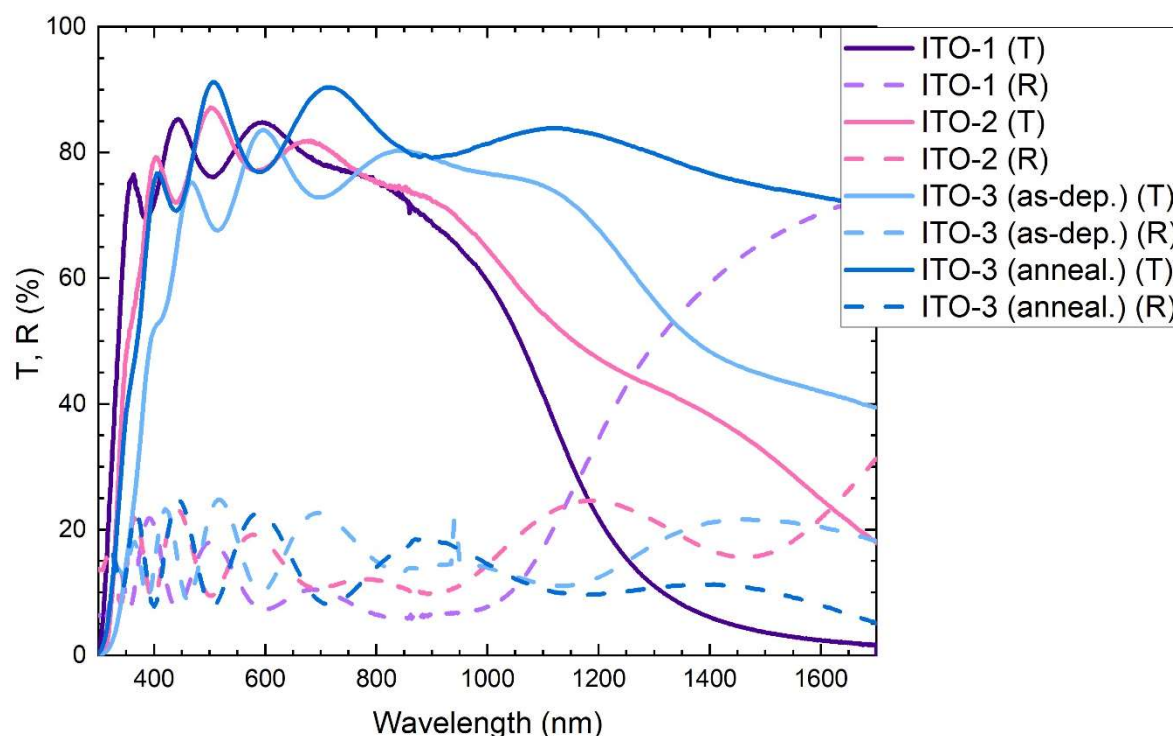


Figure 4 Transmittance (T, solid lines) and reflectance (R, dashed lines) as a function of wavelength for four different ITO substrates used for ACIGS deposition in this thesis. The optical properties were studied before ACIGS deposition on the substrates.

Before absorber deposition, the standard procedure at the Uppsala lab is to evaporate a precursor layer of NaF on top of the back contact. The standard thickness for Mo substrates is 12 nm NaF. This amount has been optimized for $\sim 2 \mu\text{m}$ absorbers deposited at 550°C on standard Mo substrates. It was found that 6 nm NaF was a better amount when working with absorbers of thickness to $\leq 1 \mu\text{m}$, lower deposition temperatures of 450°C , and ITO substrates (performance on Mo was not drastically influenced by changing the NaF amount). Therefore, 6 nm NaF precursor thickness was the standard for the experiments presented in this thesis.

3.2. ACIGS deposition

ACIGS was deposited in an old PVD co-evaporation system from Balzer, here referred to as the BAK. The BAK has a vacuum chamber where the substrates are loaded face-down above five elemental sources. Each source is individually controlled. Se is evaporated from an effusion source and is provided in excess throughout the ACIGS deposition. The four metals, Ag, Cu, Ga, and In are evaporated from fast open boat sources, with their evaporation rates controlled by mass spectrometry (MS) feedback. A schematic figure of the BAK is presented in Figure 5. Note that the figure is missing the Ag-source and that the sources are currently arranged in the order: Se, Ag, Cu, In, Ga.

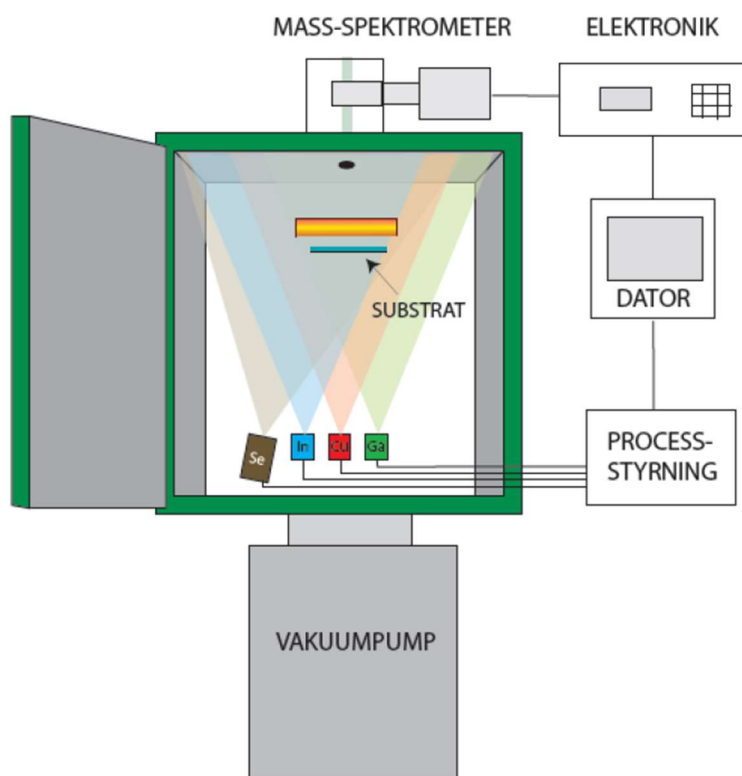


Figure 5 Graphic of the PVD co-evaporation system BAK, including the vacuum pump, the chamber with the evaporation sources, the substrate and heater, the mass spectrometer, as well as the electronics, computer and process control necessary to run a deposition.

The substrate is heated from the backside with a graphite block. The actual substrate temperature cannot be monitored during deposition, since it would interfere with either the deposition or the heating of the substrates, thus only the temperature of the graphite block is monitored by a

thermocouple mounted in a hole in the graphite block. Temperature calibration has shown that in the range of $T_{\text{graphite}}=450 - 550^{\circ}\text{C}$ the temperature on the front side of the substrate (glass) is 80 - 100°C lower. Thickness of the substrate, the type of back contact, and how quickly the temperature is ramped up will also affect the actual substrate temperature, but $T_{\text{substrate}} = T_{\text{graphite}} - 100^{\circ}\text{C}$ in steady-state is believed to be a good approximation.

The sample placement with the reference pieces (used for composition measurement by X-ray fluorescence (XRF) after each deposition) as seen from the top of the BAK is illustrated in Figure 6. The illustration shows how four 2.5*5 cm² samples can be fit in-between two XRF reference pieces of the same size. The bottom half of the samples is usually cut off after CdS deposition, but before the full cell stack has been deposited, to use as reserve pieces for characterization measurements. The compositional gradient and thickness gradient are shown with the arrows, indicating that the A-samples will be thinner and contain more Ag and Cu than the B-samples. Because of the compositional gradient, reference pieces for XRF measurements, from which the composition is then extrapolated to the samples in-between, are included at both ends of the substrate holder.

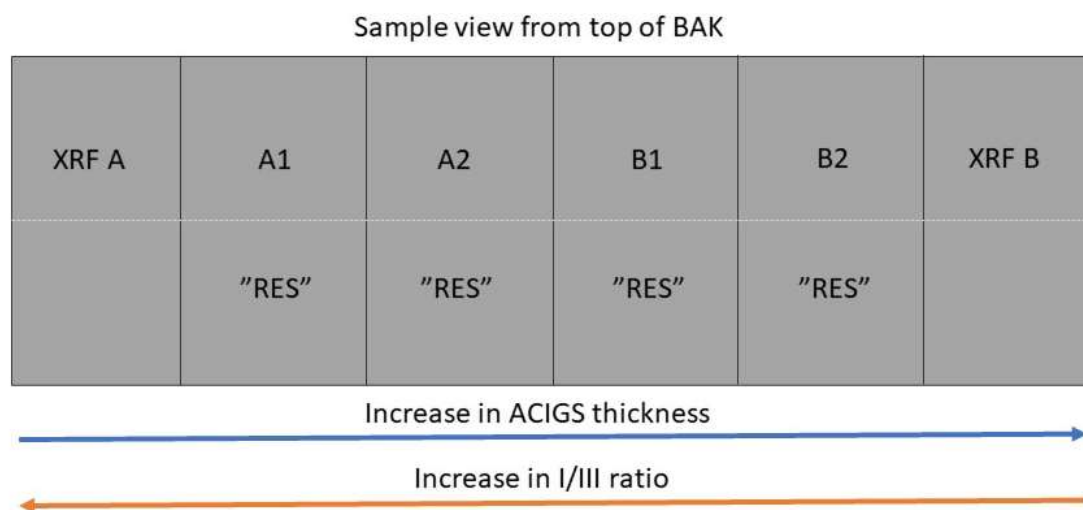


Figure 6 View from the top of the BAK of the loaded rack with samples. The XRF reference pieces are placed at either end of up to four 2.5*5 cm² samples. From left to right, the samples are named: XRF A, A1, A2, B1, B2, XRF B. The A-pieces are closer to the group-I sources, and the B-pieces are closer to the group-III sources, leading to the formation of a I/III gradient increasing from right to left. The thickness gradient from left to right is due to the Se source being closer to the A-side, blocking the other metal vapours from reaching the substrate evenly. The bottom half of the samples is treated as reserve pieces and usually not used for deposition of the full solar cell stack.

For the experiments presented in chapter 4, ACIGS of thicknesses varying from 250 nm to 1 μm were deposited. Multistage co-evaporation was used, where Cu and Ag were provided throughout the deposition, and with the substrate reaching maximum temperature during the Cu-rich stage. The shape of the Ga-grading was controlled by varying the rate of In and Ga during deposition. The resulting compositional profiles were investigated with Glow-discharge optical emission spectroscopy (GDOES).

The maximum temperature that the substrates reached during deposition was set to $T_{\text{substrate,max}}=450^{\circ}\text{C}$ to limit GaO_x growth at the ACIGS/ITO interface, and to achieve a sharply graded profile in the thin absorbers.

Sample composition was determined with XRF. Because of variations in the environment of the deposition chamber and the melting rate of the sources, there is a compositional drift between each deposition run. The XRF values were used to relate the deposition rates to a composition, and to calibrate the deposition profile with respect to the drift in mass rates.

3.3. RbF treatment

RbF was used in one experiment to study its effect on V_{OC} and FF of ACIGS on ITO. RbF was evaporated from a Radak II source with a separate shutter in the BAK chamber, without breaking vacuum, after cooling the substrate down to 300°C and letting the Se source cool down to prevent further Se addition to the absorber. The RbF source was heated up during the ACIGS deposition. The RbF thickness was controlled with a quartz crystal microbalance (QCM). After opening of the RbF shutter and reaching the desired deposition rate, the main shutter in front of the substrates was opened and the RbF PDT started. After RbF evaporation, the substrate was cooled down below 100°C before removing it from the BAK for further processing.

3.4. Buffer and window layers

CdS deposition was performed with CBD. Premixed solutions of Ammonium hydroxide, cadmium acetate and thiourea were mixed in a beaker, into which the samples were immersed, and the beaker with samples was placed up in a 60°C water bath. The process time was varied from 6 to 8 minutes from placing the beaker with room temperature solution in the water bath. A thick (~50 nm) CdS was used as standard (8-minute process), while a thinner (~30 nm) CdS was used for the ACIGS that had RbF PDT (6-minute process).

AZO and intrinsic ZnO (i-ZnO) were deposited by RF magnetron sputtering from compound targets using Ar as sputter gas in a load-lock sputter system (von Ardenne sputter, model CS730). The total window layer thickness of approximately 200 nm resulted in sheet resistances of 35-50 Ohm/Sq.

3.5. Cell definition and contacting

Cell definition was done with photolithography since this method gives more reproducible results and is less prone to cause shunts compared to mechanical scribing on ITO (mechanical scribing works well for conventional (1.5-2 μm thick) CIGS on Mo-coated substrates). 16 cells in a 4 by 4 pattern were defined on each sample. After photolithography, the final steps to prepare the cells for electrical characterisation was to mechanically remove the ACIGS with a scalpel to expose the back contact in an area outside of the cells. The exposed back contact was then soldered with indium for better electrical contact to the back contact. Laser scribing was also tested for providing a connection to the ITO, but this method requires further optimisation to ensure the same reproducibility and FF as with mechanical removal of the ACIGS and subsequent indium soldering. In the work presented in this thesis, front grids were not used for the cells.

3.6. Electrical and optical characterization

The standard performance measurement that was done for all cells was a current-voltage (IV) sweep under Standard test conditions (STC) – illumination with the AM1.5 spectrum at an irradiation power of 1000 W/m^2 (1 sun) while maintaining a cell temperature of 25°C . Four-point contacting measurements were used to avoid effects of series resistances in the probes as well as contact resistances [59]. The IV measurements were performed with a G2V Pico™ Small Area LED Solar Simulator. The samples were kept at about 25°C with a home-built Peltier element and water-cooled sample stage.

External Quantum Efficiency (EQE) was measured with a home-built system using chopped monochromatic light from a Xe lamp. For the case of low-bandgap ACIGS ($E_g \sim 1.1 \text{ eV}$) the relevant wavelength interval is up to 1150 nm , for Ga-free ACIS ($E_g \sim 1.0 \text{ eV}$) the interval is up to 1250 nm . If the effective bandgap is not known before the EQE measurement, it is safer to sweep up to 1250 nm . Additionally, tail states can introduce absorption below the bandgap, which motivates further extending the wavelength interval up to $1250\text{-}1300 \text{ nm}$. The lower limit for the interval is rarely zero, because the window layer of the ACIGS cells will absorb light above the bandgap of CdS and AZO without contributing to charge generation. Therefore, the EQE sweep in our case was done between 330 nm and 1300 nm .

All cells on ITO substrates were measured against a matt black background during IV and EQE to avoid the performance being influenced by external reflectance.

For rear IV and EQE measurements, the sample and probes were fixed to a stage that was turned upside down under the light-source, which was kept at the calibrated distance from the sample. Because of the stage, the sample could not be cooled during rear measurements, so these measurements were only done for the best-performing cells of each sample and the heating was limited by minimising the time of exposure to the full 1 sun light-intensity.

Capacitance-voltage (CV) and capacitance-frequency (admittance) measurements were performed with an Agilent 4284A Precision LCR Meter and Keithley 2401 Source Meter at room temperature in dark conditions. Four-point measurement probes were used and were mechanically connected to the front and rear contact of the cells. The methods were used to measure the doping and depletion width of ACIGS cells, and to investigate the existence of room-temperature current-collection barriers.

Photoluminescence (PL) measurements were used to study the luminescence yield of ACIGS solar cells with different Ga-gradings, and to compare the PL yield of cells on ITO and Mo back contacts. PL analysis was first performed at the Ångström Myfab laboratory with the FLS 1000 custom system from Edinburgh Instruments. A more detailed analysis with hyperspectral imaging, using a system from Photon ETC, was later conducted at the French research institutes CNRS-IPVF by fellow PhD student Klara Kiselman.

3.7. Material characterization

Elemental composition of the absorbers was measured by XRF with model Epsilon 5 from PANalytical. The measurements were done after each deposition run. Due to the position of the metal sources in relation to the substrates in the BAK chamber, there is always a compositional gradient and thickness gradient introduced. Therefore, XRF was measured on reference pieces with Mo on glass placed at either end of the other substrates. The compositional values were then extrapolated for the substrates in-between the pieces measured in the XRF.

The XRF measurement spectra of the ACIGS absorbers were compared against a known reference ACIGS sample, with similar but not identical composition. An uncertainty in determining the sample composition is introduced due to the difference in thickness and composition between the samples and the reference. With absorber thickness decreasing, the attenuation of the XRF signal for the elements decreases at different rates, which makes the comparison with the reference sample (which is 2.5 μm thick) less valid. In general, the concentration of elements with characteristic fluorescence radiation of lower energy are overestimated for thinner samples compared to the reference sample. When composition is presented in this thesis, the ratio I/III might therefore appear more off-stoichiometric than the usual target for ACIGS, but this is simply because of the offset introduced by the reference sample being much thicker than the samples deposited in the presented experiments.

GDOES measurements were performed with model GDA 750 HR by Spectruma to attain elemental depth profiles. This was used to compare the Ga-gradings formed in the absorbers during different process conditions and when different substrates were used. XRF values of the average absorber composition were used to calibrate the GDOES mass ratios.

For analysis with electron microscopy, thin lamella samples were prepared by cutting with Ga-based Focused Ion Beam (FIB) in the ZEISS Crossbeam550. STEM and STEM with Energy Dispersive X-ray Spectroscopy (STEM-EDS) analysis were performed at 200 keV in the SuperX G2 detector, model Titan Themis 200 (Thermo Fisher Scientific). In the work presented in this thesis, STEM was used to study thin cross-sections of the ACIGS material and the back contacts. STEM-EDS was used to study the Ga-grading and, with the high-resolution images from STEM, identify layers of GaO_x . While STEM is a high-resolution technique, it is limited in that it can only capture a small area of the sample, which is not always statistically representative of the whole sample.

4. Research highlights

The focus of this chapter are the studies of ACIGS solar cells performed as part of this thesis. It begins by introducing a study of optimising the solar cell process for ACIGS on ITO back contacts. This is followed by a study comparing Mo and ITO back contacts for thin ($\leq 1 \mu\text{m}$) ACIGS absorbers. This study also investigated the effect of different Ga-gradings and absorber thicknesses on cell performance. The results of the comparison between Mo and ITO, as well as the Ga-gradings, were first presented at the IEEE PVSC 53rd conference in Montreal, and sent in as a manuscript to IEEE Journal of Photovoltaics [60], which can be found attached to the thesis. In addition to these results, this chapter presents some further unpublished studies made of ACIGS solar cells on ITO back contacts, including a RbF PDT experiment.

4.1. Optimising the ACIGS process for ITO back contacts

The ACIGS deposition process had to be adapted to the change of substrates from Mo to ITO. As mentioned previously, GaO_x formation can deteriorate performance on ITO, and the growth of this layer is catalysed by NaF and temperature. A study was therefore conducted to optimise the NaF pre-deposition treatment and the maximum temperature reached during ACIGS deposition. The study was conducted with ultrathin (~ 500 nm) ACIGS with no intentional Ga-grading to better see the influence of the rear of the device on the performance. The ITO-1 and Mo substrates in Table 1 were used. NaF of standard, 12 nm thickness was applied, as well as a thinner layer of 6 nm. Standard deposition temperature of 550°C and the lower deposition temperature of 450°C were tested. The resulting performance of the 8 different types of samples, prepared in two separate deposition runs on the same day, are presented in Figure 7.

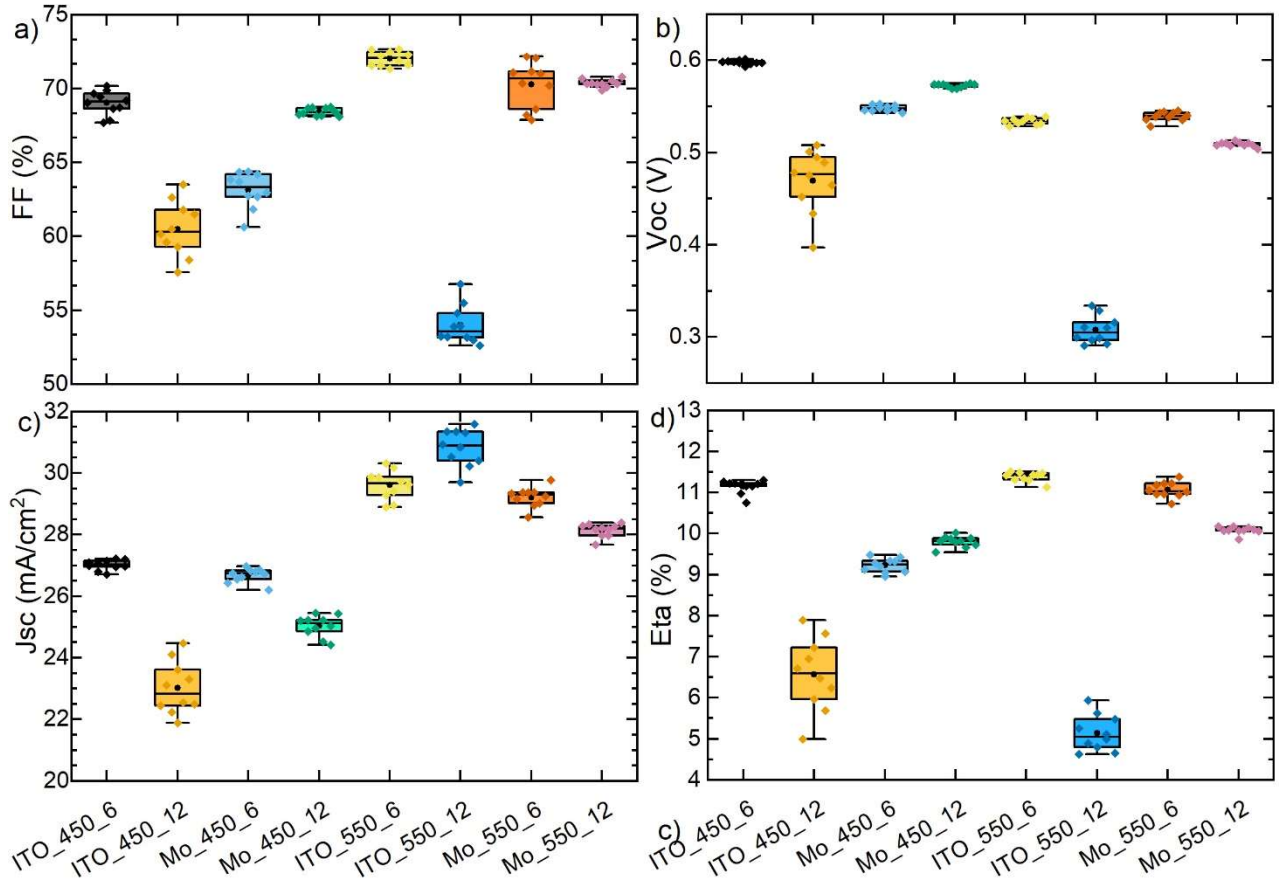


Figure 7 Boxplots of a) FF, b) Voc, c) Jsc, and d) efficiency (Eta) from the optimisation study of NaF treatment and deposition temperature. The names at the bottom indicate the substrate, temperature in degrees centigrade, and NaF thickness in nm pre-deposition. The boxplots show the median and the percentiles of each sample, the black circles are the mean values for each sample, and the diamonds superimposed on the boxplot represent each cell measurement value.

The thinner NaF layer resulted in the best performance on ITO, and this performance exceeded that of cells made with the standard process on Mo. Due to variations in the composition across the samples, and small variations between runs, the effect of NaF and temperature was not always reproducible. For example, the ITO with 12 nm NaF was most likely group-I rich, which

deteriorates its performance in addition to the effects of temperature and NaF thickness. A later replica run of the 450°C run showed improved performance of the two ITO samples. The replica run resulted in ITO with 6 nm NaF even reaching close to 14% efficiency and voltages above 0.6 V, and the ITO sample with 12 nm NaF performing on par with the Mo sample with 6 nm NaF. It was concluded that for the thin ACIGS on ITO the record performance was achieved with the thinner, 6 nm NaF layer and the lower deposition temperature of 450°C, therefore these parameters were chosen for the optimised ITO process.

For ACIGS deposited at higher temperatures on ITO we expected the GaO_x-formation to be more significant. A higher degree of interdiffusion between Ga and In was also expected. GDOES measurements provided in the appendix (see Figure 22 and Figure 23) showed that an increase of Ga at the back contact happened with the 12 nm NaF precursor layer, and although it was further enhanced in the high temperature case, temperature itself did not cause an aggregation of Ga at the back. It is not certain that the increased Ga-concentration can be connected to an increased GaO_x-formation, since the GGI increased at the Mo/ACIGS interface as well, and it was later seen that GaO_x thickness does not increase with more Ga present at the back. A decreasing V_{OC} and a change of bandgap (compare EQEs in Figure 21 in the appendix) was observed for the cells on ITO at higher temperatures, indicating a higher parasitic reaction at the back contact, but no blocking behaviour was seen.

4.2. Comparing Mo and ITO back contacts

ACIGS cells of thicknesses 550-650 nm were prepared on ITO and Mo back contacts with the method described in chapter 3, now with a Ga-grading of the absorbers. The process temperature and NaF precursor had been optimised in the study described above in chapter 4.1 to yield good cell results for thin ACIGS on ITO. This meant that the maximum deposition temperature was lowered to 450°C, NaF precursor thickness was lowered to 6 nm, and photolithography was used to define the cells to avoid introducing shunt paths between the cells. The motivation to have thin absorber thickness was to make the rear surface, and thus the back contact, have more influence on the performance of the solar cells for clearer comparison. Therefore, we did not expect to reach the highest efficiency. The Mo samples were made as references in the same runs as the ITO samples.

In Figure 8 the performance parameters from JV-measurements are presented for the best cells on ITO and Mo made in the study. The best cell efficiencies were 15.2% for the 650 nm ACIGS on ITO back contact, and 15.0% for the 650 nm ACIGS on Mo. It was found that cells on ITO back contacts performed statistically better than cells on Mo back contacts [60]. Especially interesting was the find that there was no FF loss, but rather a gain in FF, when using the ITO compared to Mo. The only parameter where the Mo cells performed better than ITO was in J_{SC}, likely due to the internal reflection from the Mo surface.

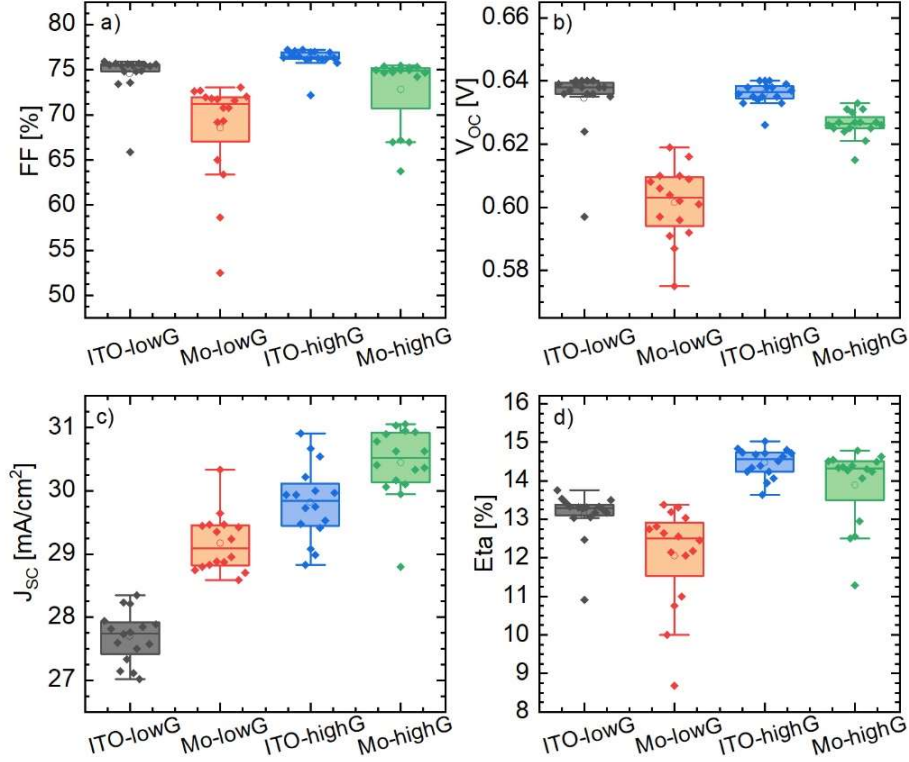


Figure 8 Boxplots of a) FF, b) V_{oc} , c) J_{sc} , and d) efficiency (Eta) for the best ACIGS sample on ITO and on Mo with two different Ga-gradings, one with low Ga (-lowG) increase and one with high Ga (-highG) at the back contact. The boxplots show the median and the percentiles of each sample, the circles are the mean values for each sample, and the diamonds superimposed on the boxplot represent each cell measurement value.

The study tested two profiles with different Ga-gradings, one with lower Ga increase at the back (samples ITO-lowG and Mo-lowG) and one with higher Ga increase at the back (samples ITO-highG and Mo-highG). The samples with high Ga at the back were un-intentionally about 100 nm thicker than the samples with low Ga at the back, which can have influenced the performance by increasing absorption. Table 2 explains the names of the samples and briefly describes their differences. The Ga-gradings will be further discussed in the chapter 4.3.

Table 2 Description of samples used in the experiments in the IEEE manuscript [60]. Details about the substrates are listed in Table 1.

Sample name	Substrate	Compositional profile	ACIGS thickness
ITO-lowG	ITO-1	Low Ga-grading	550 nm
Mo-lowG	Mo	Low Ga-grading	550 nm
ITO-highG	ITO-1	High Ga-grading	650 nm
Mo-highG	Mo	High Ga-grading	650 nm

The success of the ITO cells is attributed to the ACIGS process, which allowed for a well-defined Ga-grading to be formed without a detrimental amount of GaO_x at the ITO back contact. STEM and STEM-EDS analysis of the samples was used to identify a <3 nm thick GaO_x layer at the ACIGS/ITO interface for both Ga-gradings. No GaO_x was identified in the samples on Mo, which led to the conclusion that the GaO_x layer at the ITO is contributing to rather than deteriorating

the performance of ACIGS solar cells. Since both FF and V_{OC} were higher for the ITO cells than the Mo cells, this points towards a better passivation of the back contact in the ITO cells. A reasonable assumption is then that the GaO_x layer has a passivating effect on the back contact, and that this effect is better than the passivating effect of the $MoSe_2$.

Although these findings are surprising, considering previous reports of loss in FF and the detrimental effect of GaO_x , Nakada et al. showed as early as 2002 that ITO could work just as favourably as Mo with CIGS [44]. Their hypothesis was then that the ITO/CIGS interface can have a favourable alignment of the VB and CB, or that the thin barrier that can form at the interface allows for tunnelling. GaO_x has known passivating effects, and has been used to passivate the front interface between CIGS and CdS [45]. The difference at the rear interface is that there GaO_x creates a hole barrier. Following the logic of Nakada et al., it could be claimed that a process which limits the thickness of the GaO_x layer to allow for holes to tunnel through the barrier would gain a favourable ohmic contact, and a passivated rear interface, at the ITO.

4.2.1. Additional characterisation with CV and PL

In addition to the measurement results presented in the manuscript, CV measurements were performed on some of the ACIGS cells on Mo and ITO made in the study. Absorber material from the same samples, using an area that had only been covered with ACIGS and CdS (the reserve pieces in Figure 6), were analysed with PL. Ideally, one wants to measure the PL of the absorber material only, but the CdS is needed to prevent the ACIGS from oxidising and it is transparent to the emission peaks from ACIGS.

CV measurements showed no clear difference between Mo and ITO samples. Depletion widths were calculated to be around 0.15-0.2 μm , except for two outliers at 0.3 μm (both on Mo), see Figure 9. From this measurement it could be determined that the devices were not fully depleted at zero bias. No barriers at room temperature could be identified in admittance measurements, which was as expected since the devices were high-performing.

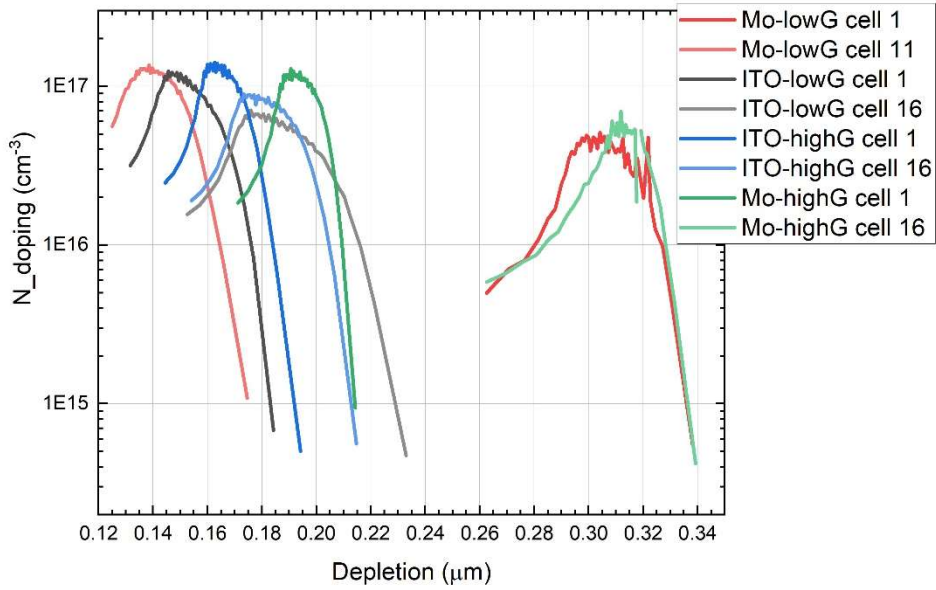


Figure 9 Doping concentration plotted against depletion width, measured during a CV forward voltage bias sweep, for two cells on each sample: Mo-lowG (red), ITO-lowG (black), ITO-highG (blue), Mo-highG (green).

The PL hyperspectral imaging measurements revealed several trends. Firstly, the PL peak intensity was higher for the ACIGS samples on Mo compared to ITO when comparing the case of the high Ga-grading. In Figure 10a) the samples Mo-1B1 and Mo-1B2 are more luminescent (higher value from integrated PL peak) than ITO-1A1 and ITO-1A2 which are all made with the same absorber with high Ga-grading. This was unexpected, since the ITO samples performed better in V_{OC} and a more intense luminescence peak is usually correlated to a higher V_{OC} . A possible explanation for the difference in peak intensity could be that Mo is reflecting some of the emitted light, which is increasing the height of the PL peak, or that the ITO, being transparent, is transmitting or absorbing some of the emitted light. A different explanation is that the material in the ITO samples had deteriorated during the time that the samples had been stored before the PL measurements were performed. This deterioration will be further discussed in the chapters 4.7 on stability. A second trend, which is seen in Figure 10b), is a gradient across the ITO samples, showing that the PL peaks occur at different wavelengths across the samples. This will be further discussed below.

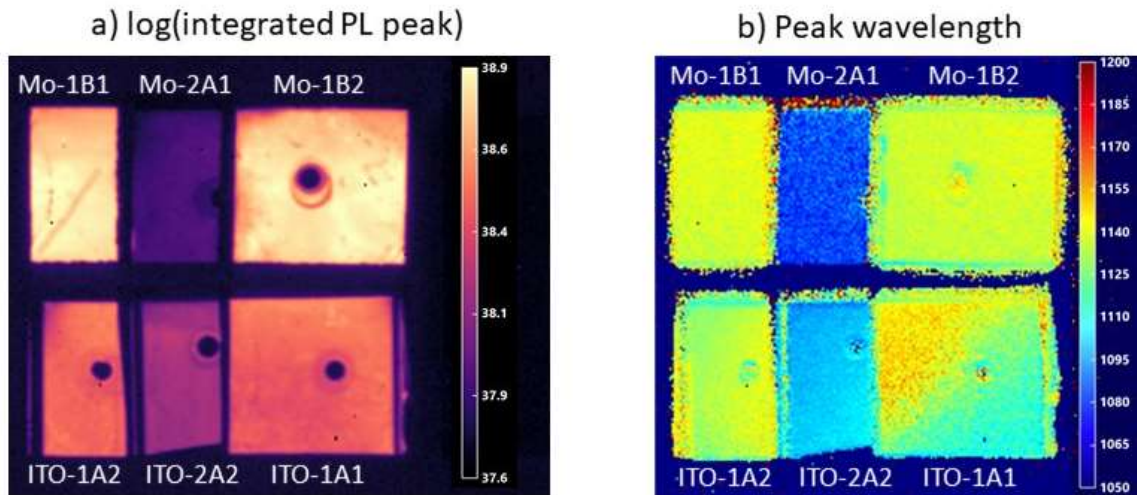


Figure 10 Maps of PL taken with hyperspectral imaging. Subfigure a) is showing the logarithm of the integrated PL peaks at each point of the samples. Subfigure b) shows the wavelength of the PL peaks at each point of the material. Mo-1# and ITO-1# samples have the ACIGS absorber with high Ga-grading, while Mo-2A1 and ITO-2A2 have ACIGS absorbers with low Ga-grading. The sample name indicates the position in the BAK sample rack (see Figure 6). The non-luminescent circles on the samples are GDOES craters.

Figure 11 presents an average PL peak for the four different samples: ITO-lowG, Mo-lowG, ITO-highG, and Mo-highG. For the case with the low Ga-grading, the peak intensities do not follow the trends observed for the high Ga-grading, with the PL peak on the Mo sample in this case being much lower than the PL peak on ITO. As can be seen in Figure 10, the Mo-2A1 sample is barely luminescent, indicating some deterioration of the material, which is not necessarily connected to the Ga-grading.

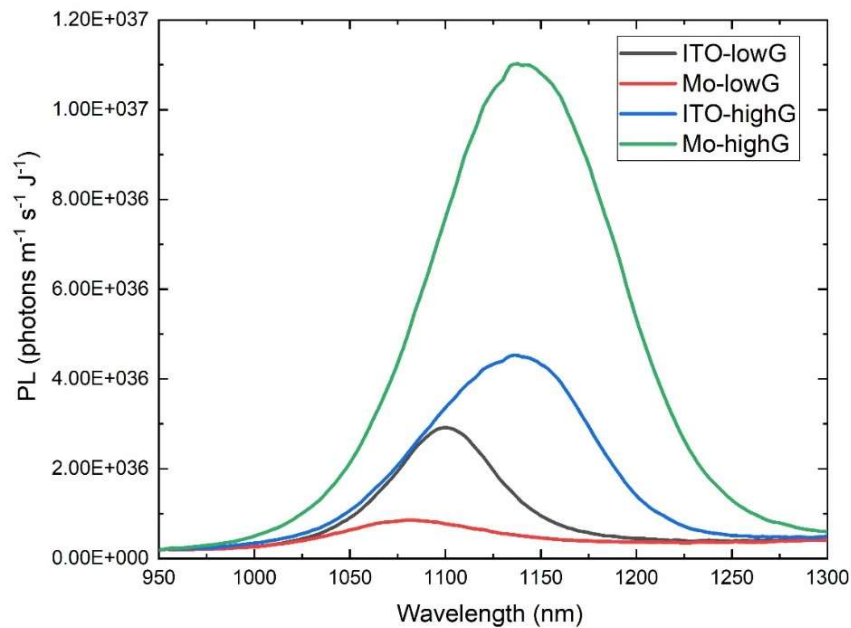


Figure 11 Average PL peaks plotted from measurements with hyperspectral imaging for ITO-lowG (black), Mo-lowG (red), ITO-highG (blue), and Mo-highG (green).

Figure 10 and Figure 11 show that the intensity for the low Ga-grading absorber is lower than for the high Ga-grading, and there is a slight shift in wavelength of the peak intensity. The shift of the peak wavelength indicates a small shift in bandgap (a shift from 1100 nm to 1150 nm is equal to a bandgap difference of 0.05 eV), which can also be seen in the EQE absorption edge in the manuscript [60]. The increase in PL intensity is not obviously connected to the electrical performance, because the change in V_{OC} from the lowG to highG samples was not that dramatic. However, the increase PL yield is an indication of decreased non-radiative recombination, likely resulting from the increased Ga-grading.

As already mentioned, the PL peaks shifted in wavelength across the ITO samples, while on the Mo samples this trend was not observed. Figure 12 shows the PL peaks taken along the diagonal of one of the ITO samples, illustrating how the one peak successively gains a shoulder (or forms a double peak). The shift in PL peak wavelength across the ITO samples is believed to be caused by a phase segregation across the sample, which could also explain the lower average PL peak intensity if the phases are not equally luminescent (the intensity decreases with the peak shift in Figure 12). This phase segregation is more likely to have happened in the ITO samples because of their position as the #A1 and #A2 samples in the deposition chamber, which could introduce a group-I rich or Se-rich phase. The existence of this phase is further supported by the poor PL performance of the Mo-2A1 sample, where this secondary phase could have been dominant.

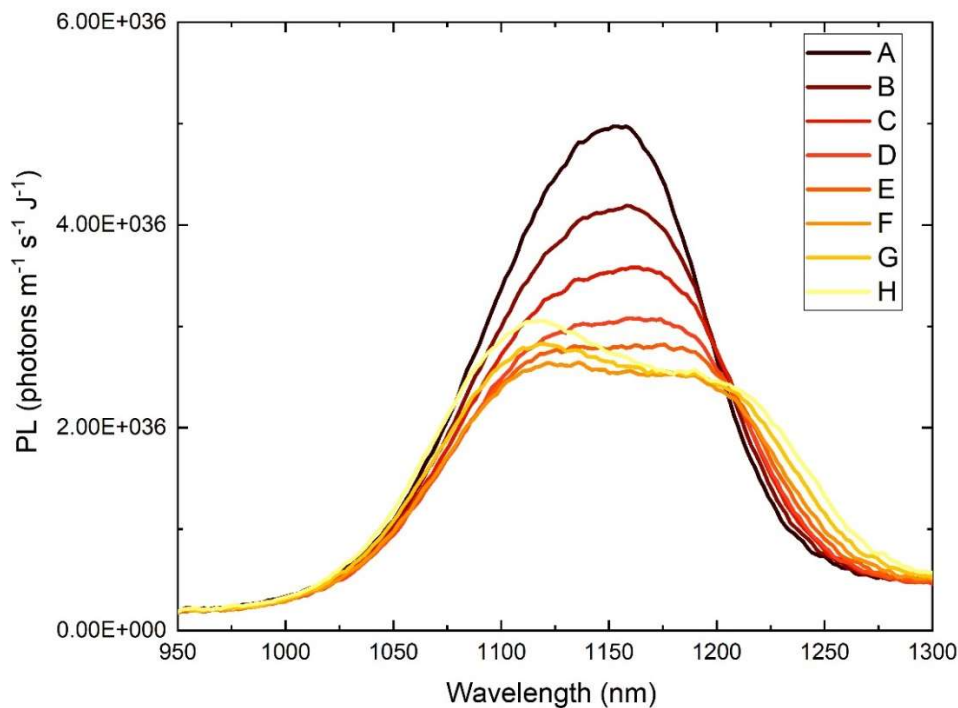


Figure 12 PL peaks measured along the diagonal of the ITO-1A1 sample, with peak A being in the top-left corner and H being in the bottom-right corner (as oriented in Figure 10). The main peak shifts towards shorter wavelength after peak F, and a clear shoulder appears at longer wavelengths. The peaks are also broadening towards longer wavelengths.

4.3. Ga-graded ACIGS on ITO

Different Ga-gradings of ACIGS were studied by varying the GGI-ratio in the beginning of the absorber deposition as compared to the next stages. Figure 13a shows the evaporation rates of the elemental sources as a function of deposition time during the multistage deposition, while subfigures b) and c) show the resulting GGI calculated from GDOES measurements. Three different profiles, which all included Ag and Cu, are shown: no Ga-grading (flat), low Ga-grading (Ga1 and In1), high Ga-grading (Ga2 and In2). To achieve a constant GGI (flat Ga-grading) throughout the absorber grown on ITO it was still necessary to increase the GGI a little bit in the beginning of the deposition to compensate for the GGI decreasing as a result of GaO_x formation.

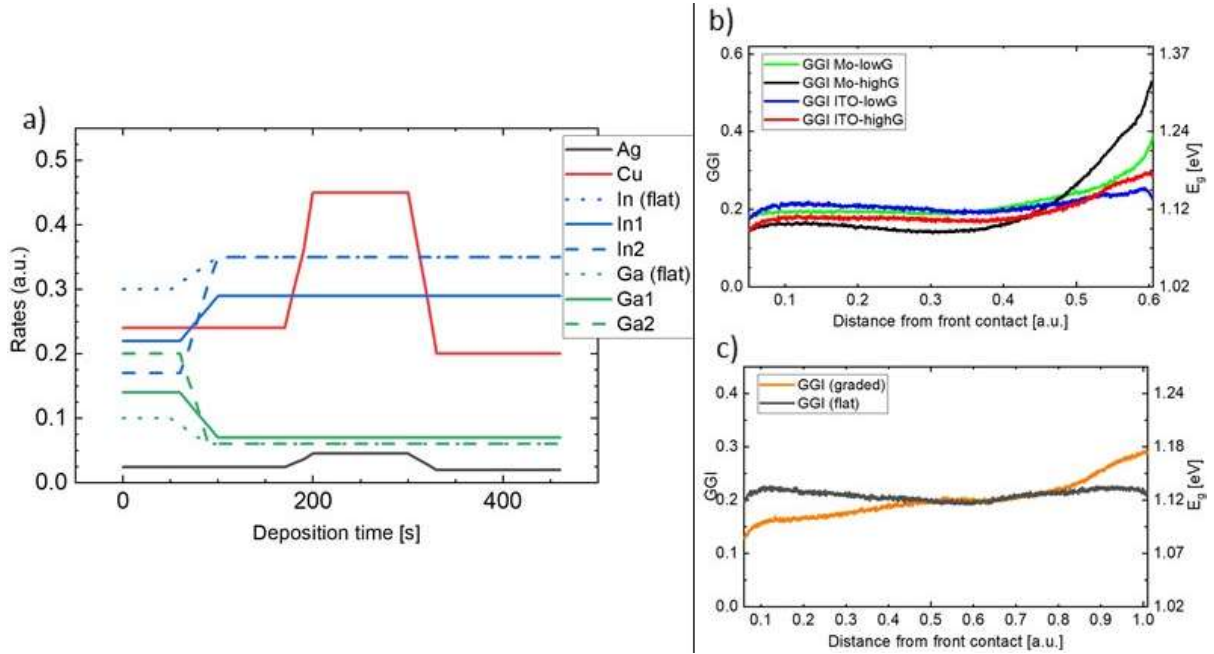


Figure 13 a) Evaporation rates as a function of deposition time for three different profiles: flat GGI, low GGI increase at back contact (#1), high GGI increase at back contact (#2). b) The GGI profiles, calculated from GDOES measurements for profiles 1 and 2 on ITO (blue and red lines) and Mo (green and black lines) back contact. c) The GGI profiles of 1 μm ACIGS with a graded profile (profile 2) and a flat profile. Figures reprinted from [60], copyright © IEEE.

When comparing to references on Mo, the Ga-grading looks less defined in ACIGS on ITO. However, one should be careful when comparing the absolute values of the GGI profile on Mo and ITO since the compositional values were calculated from XRF measurements made on Mo reference samples. Since the ITO back contact contains In, it is safe to say that this can influence the absolute GGI value of the ACIGS. Additionally, the formation of GaO_x takes oxygen from the ITO and makes indium available to the CIGS film to replace the gallium, lowering the GGI at the ITO back contact, which will not happen on the Mo back contact. It is still relevant to compare the relative shape of the Ga-grading and to compare performance of ACIGS with different height of the Ga-grading.

Referring again to Figure 8, the higher Ga-grading (profile 2) performed better in overall efficiency and J_{sc} , although this could also have been an effect of the thickness increase. For the Mo samples there was an increase in V_{oc} , which was not seen for the ITO samples. A small FF increase could

also be noted for the samples with high Ga-grading. As it was mentioned in chapter 4.2, the same thickness of GaO_x was identified for both profiles, despite the difference in Ga concentration at the back contact. The profile with high Ga was chosen as the standard profile for the following experiments.

To further study the effect of the Ga-grading, two profiles were prepared for a 1 μm absorber, one with a Ga-grading that increased towards the back and one with a constant GGI (flat profile) throughout. The GGI profiles are presented in Figure 13c. To be able to make the comparison, the average composition of the two absorbers was designed to be the same, resulting in the flat Ga profile having a slightly higher effective bandgap than the graded profile. The gain from the Ga-grading was significant in J_{SC} and the EQE response (both front and rear illumination) [60]. This had previously been observed for CIGS devices of standard thicknesses (1.5-2 μm), where an improved EQE for longer wavelengths was seen for absorbers with a GGI that increased towards the back [34]. For thinner devices, improvements in V_{OC} and FF with the same type of Ga-grading had also been observed, but this was not clearly seen in our study. It is likely that the devices need to be thinner than 1 μm to achieve a more dramatic effect on V_{OC} and FF with the Ga-grading (which we can somewhat see when comparing the studies in 4.1 (no intentional grading) and 4.2 (with Ga-grading)). However, with the higher effective bandgap for the ungraded absorber, an increase in V_{OC} would have been expected unless the decreased surface passivation caused a V_{OC} loss. It can be concluded that the Ga-grading has a passivating effect that increases current collection for a range of absorber thicknesses, and possibly decreases losses in V_{OC} and FF for ≤ 1 μm thick absorbers.

4.4. Absorber thickness

ACIGS cells of thicknesses 250-1000 nm on ITO back contacts were studied under front and rear illumination [60]. Cells were made on substrates of type ITO-1 and ITO-2, described in Table 1. The best performing cells of each thickness are presented in the following graphs.

Increasing the absorber thickness increased the J_{SC} and the EQE response for longer wavelengths under front illumination, see Figure 14. There was however a loss in V_{OC} and FF observed for the best 1 μm devices compared to the best devices at 500-650 nm. A possible explanation for this loss could be increased bulk recombinations in the thicker absorber compared to the 500 nm absorber. The 250 nm absorber had the lowest V_{OC} and front J_{SC} . The former likely due to increased

recombination at the rear surface, and the latter due to incomplete absorption.

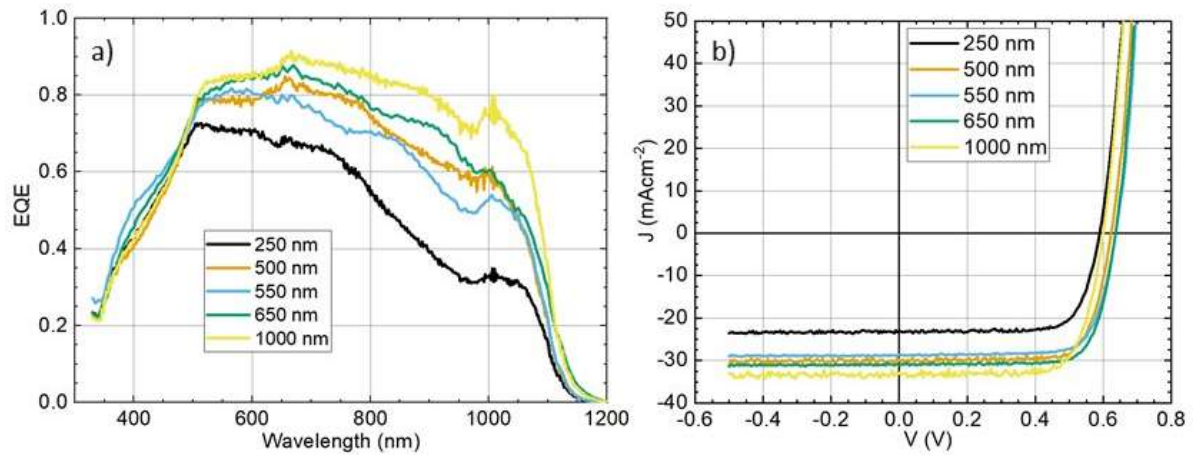


Figure 14 a) EQE curves and b) JV-curves of cells with absorber thicknesses of 250 nm (black), 500 nm (orange), 550 nm (blue), 650 nm (green), and 1000 nm (yellow) on ITO. The EQE response is shown to increase for wavelengths above 500 nm with each thickness increase, which increases the J_{SC} as seen in subfigure b). The V_{OC} is lower for the absorber thicknesses 250 nm and 1000 nm compared to the 500-650 nm absorbers.

The EQE and JV measurements under front and rear illumination for the absorbers of 250 nm, 500 nm, and 1000 nm are presented in Figure 15. It was observed that the EQE response under rear illumination shifted towards longer wavelengths with increased absorber thickness. The thin absorber had the highest J_{SC} under rear illumination and the highest bifaciality factor, which can be explained by the short distance between the generation of carriers and the SCR. For the thinnest device the low EQE response for long wavelengths can be explained by absorption loss, while there is comparably good collection for the short wavelengths. The absorption loss could also be caused by parasitic absorption in the ITO. The latter becomes more evident for the thicker absorbers, which both have low EQE response for longer wavelengths. The loss of short wavelengths in the EQE response of the thicker absorbers indicates increased carrier recombination at the rear surface when the width of the quasi-neutral region is increased.

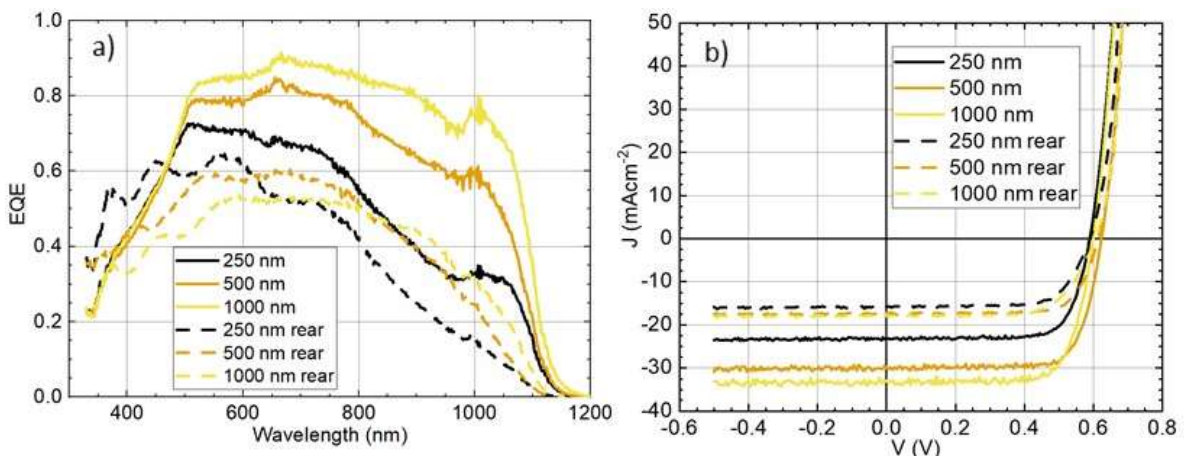


Figure 15 a) The EQE and b) JV under front illumination (solid lines) and rear illumination (dashed lines) for absorbers of thickness 250 nm (black), 500 nm (orange) and 1000 nm (yellow). Under rear illumination, the EQE response shifts towards longer wavelengths for thicker absorbers. Subfigure a) is reprinted from [60], copyright © IEEE.

4.5. Importance of NaF precursor optimisation for ACIGS on ITO

The importance of the NaF precursor layer for absorbers grown on ITO became evident when a deposition run was performed on substrates without the precursor. Figure 16 shows the JV-curves of four samples, where samples 1 and 2 were deposited in the same run and had no NaF precursor, while samples 3 and 4 were deposited in a later run and had a 6 nm NaF precursor layer. There were minor variations in the thickness and the I/III value between the two runs, while GGI was the same. The same type of ITO on SLG substrate was used for all samples. The JV curves of the samples 1 and 2 show a much lower voltage, indicating that the devices are undoped and probably fully depleted, yet the J_{SC} that is not too far from samples 3 and 4. The result clearly shows that when no NaF is added to the ACIGS process after the ITO, the cell performance suffers from lower V_{OC} and therefore lowered FF, but there was no sign of any blocking behaviour, demonstrating an adequate ohmic contact to the ITO.

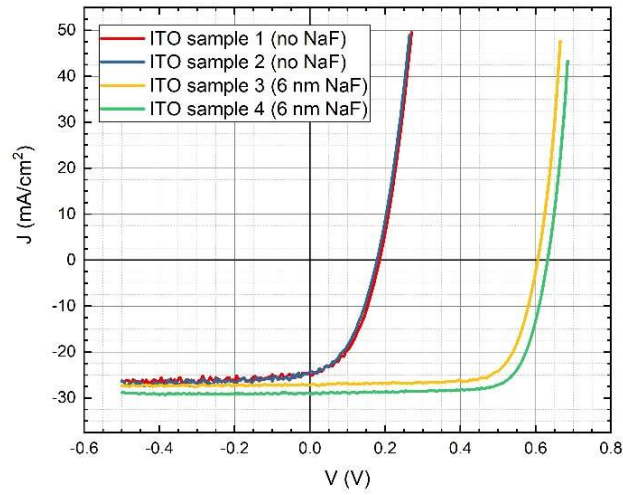


Figure 16 JV-curves for ACIGS cells from four different samples on ITO back contact: two with no NaF treatment (red and blue lines) and two with 6 nm NaF precursor (green and yellow lines). The cells with NaF precursor have improved performance, especially in V_{OC} . There is no blocking behaviour of the JV-curve for the cells without Na.

In addition to blocking Na from diffusing out of the SLG into the ACIGS, the ITO also blocks the Na from diffusing from the ACIGS into the SLG. STEM analysis of the samples ITO-lowG and ITO-highG (see Table 2 for details) showed pore-like structures at the ITO/ACIGS interface. Upon further analysis with STEM-EDS, these structures were identified to contain Na and F, see Figure 17.

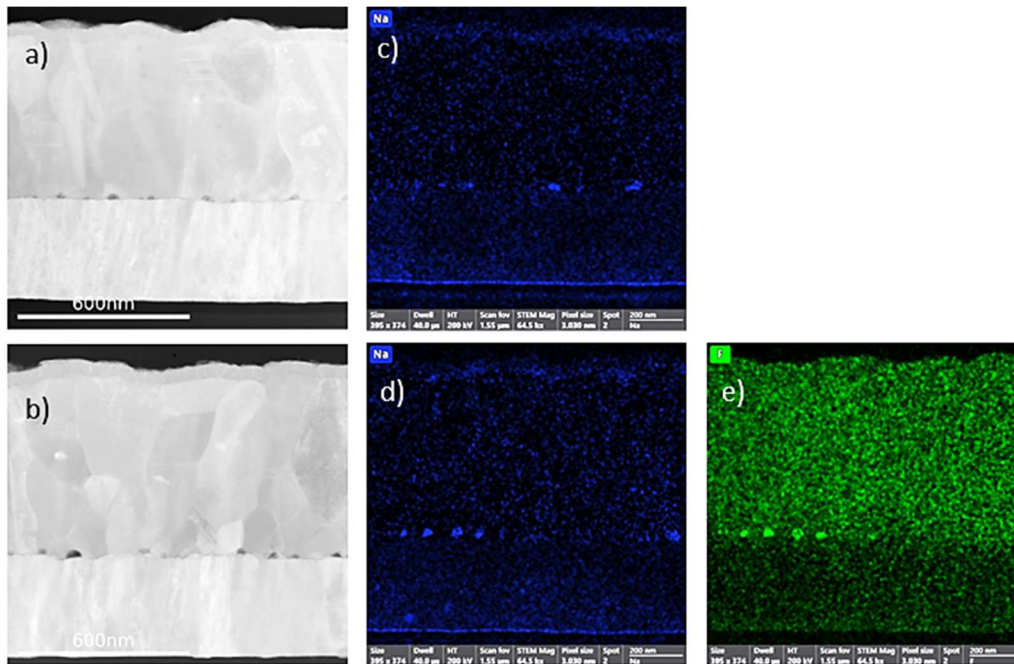


Figure 17 STEM images of ACIGS on ITO (a-b). The STEM-EDS analysis shows the sodium (c-d) concentration and the fluorine (e) concentration. The top row contains the analysis for the ACIGS absorber with low Ga-grading, and the bottom row the high Ga-grading.

Evidently, the ACIGS had become saturated with Na and the ITO blocked the excess from diffusing into the SLG. The samples on Mo back contacts did not have the pore-like structures, and the EDS revealed Na in the Mo. The Na-F structures at the ITO/ACIGS interface did not appear to have a detrimental effect on the cell performance as the cells on ITO still functioned better than the cells on Mo, where no Na-F structures could be identified.

Following the discussion above about the importance of the NaF treatment, it could be of interest to investigate the role of the Na-F structures for the electrical performance of the solar cells.

4.6. RbF PDT of ACIGS on ITO

The first experiment with RbF PDT for ACIGS cells on ITO was conducted by adding a RbF evaporation step to the standard 1 μm ACIGS process. A RbF layer of 6 nm was evaporated and the standard CdS thickness (50 nm) was deposited by CBD. The initial result, when measuring JV directly after cell processing, was a decreased performance and a clear blocking behaviour in some JV-curves compared to cells with no RbF PDT, see Figure 18. After 72h LS the performance improved and exceeded that of cells with no RbF. The LS effect was only slightly diminished after 24 h of dark storage. The improvement from RbF plus LS was mainly in V_{OC} and FF, but for some cells there was also an improvement in J_{SC} , which could be seen in the JV and EQE measurements.

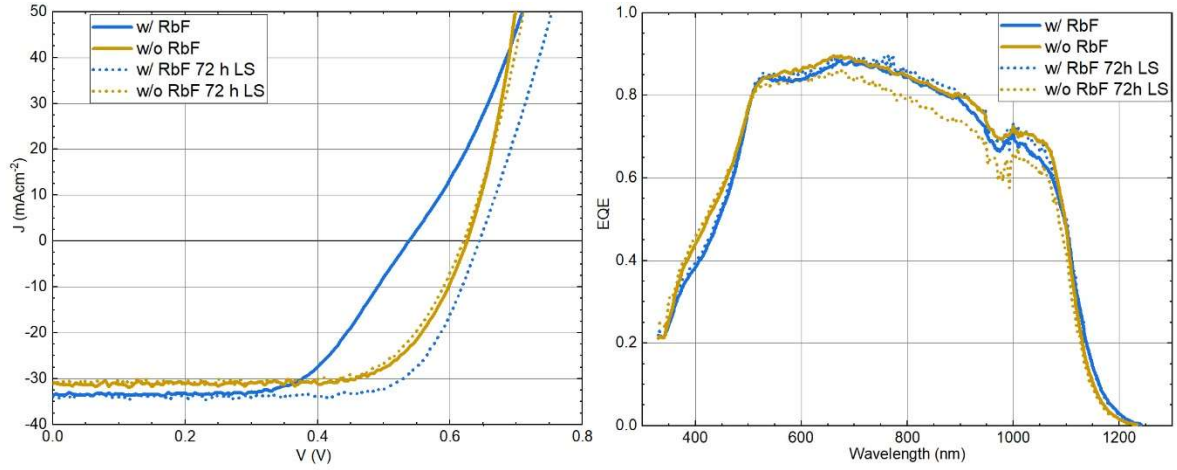


Figure 18 JV (left figure) and EQE (right figure) for ACIGS cells on the same type of ITO back contact with and without RbF PDT. The blue lines in the graphs are for the device with PDT, the yellow lines for the device without RbF. The solid lines show measurements made before LS, and the dotted lines are from measurements after 72h of LS. The LS treatment of the device with PDT increased the performance beyond the device without PDT, which was less affected by the LS.

Table 3 presents the resulting performance after LS of the best devices in this experiment. The best performance was achieved with the annealed ITO-3 substrate, treated with 6 nm RbF and LS, reaching by far the highest V_{OC} . The Mo references were performing much worse than what was expected after the comparison study in chapter 4.2. It was unclear if this was owing to these samples having the composition with the highest I/III ratio of the batch or because of the process parameters, which had been seen to negatively affect performance on Mo in the optimisation study in chapter 4.1.

Table 3 Performance and composition of the best performing solar cells after 72h LS, made in the first RbF-trial, where 6 nm RbF PDT was added during a 1 μm ACIGS run. The comparison is made with cells with no RbF PDT.

RbF PDT	Substrate	V_{OC} [V]	$J_{SC, EQE}$ [mA/cm^2]	FF [%]	PCE_{EQE}	GGI	I/III	AAC
6 nm	Mo	0.349	34.32	63.33	7.59	18	85	5
	ITO-2	0.622	33.07	74.30	15.29	18	83	5
	ITO-3 (annealed)	0.644	33.94	74.05	16.19	19	82	5
	ITO-3 (as-deposited)	0.591	32.61	71.09	13.71	19	80	5
None	Mo	0.498	34.43	59.19	10.16	19	85	14
	ITO-2	0.631	32.67	76.56	15.79	19	84	14
	ITO-3 (annealed)	0.621	32.22	71.91	14.38	20	82	13
	ITO-3 (as-deposited)	0.612	31.78	72.95	14.18	20	81	13

A subsequent RbF experiment aimed to investigate the effect of different RbF amount on the performance, as well as decrease the CdS thickness to 30 nm, and study the effect of LS on JV-parameters measured under rear illumination. ITO-2 and as-deposited ITO-3 substrates were used,

as well as Mo substrates for reference. In order to see if the Mo performance in the previous study had been influenced by the high I/III ratio, the two Mo references were now placed at either end of the sample rack, to be at different ends of the I/III gradient. The RbF thickness, deposited after ACIGS absorber deposition, was varied over three batches of samples: 3 nm, 6 nm, and 12 nm. The resulting performance of the best cells are tabled in Table 4 along with the XRF composition values of the samples.

Table 4 Performance and composition of the best performing solar cells with 1 μm ACIGS run after 68h LS from three different PDT batches: with 3 nm RbF, 6 nm RbF, and 12 nm RbF.

RbF PDT	Substrate	V_{OC} [V]	J_{SC, EQE} [mA/cm ²]	FF [%]	PCE_{EQE}	GGI	I/III	AAC
3 nm	Mo-A	0.297	35.5	57.99	5.94	18	89	8
	ITO-2	0.595	34.13	74.53	15.13	18	87	8
	ITO-3 (as-deposited)	0.552	33.26	68.67	12.63	18	84	7
	Mo-B	0.381	35.05	69.23	9.25	18	82	7
6 nm	Mo-A	0.387	34.58	64.15	8.57	17	67	10
	ITO-2	0.55	33.13	68.77	12.53	17	66	10
	ITO-3 (as-deposited)	0.405	34.84	45.54	6.42	17	63	10
	Mo-B	0.406	34.22	64.76	9.00	17	61	10
12 nm	Mo-A	0.412	35.3	66.04	9.62	16	74	10
	ITO-2	0.568	33.21	64.28	12.14	16	72	10
	ITO-3 (as-deposited)	0.532	34.92	62.95	11.71	17	70	9
	Mo-B	0.43	35.63	68.52	10.49	17	68	9

The comparison study had an added element of uncertainty because of the large compositional variation (mainly group-I) between the ACIGS runs. The run with 3 nm RbF was in the higher range of the I/III target, close to the stoichiometric limit, which can explain why one of the Mo references is performing worse than the other. The run with 6 nm RbF was particularly far from the I/III-0.83 mean target value, and thus the high performance of the previous experiment with 6 nm RbF could not be reproduced. Nevertheless, the study showed a blocking behaviour pre-LS in the JV-curves, which increased with increasing RbF thickness. The JV-curves for the best devices of each sample and batch are presented in Figure 19. After LS, the JV-curves were no longer blocked for the case of 3 nm and 6 nm, while the samples with 12 nm RbF still had S-shaped JV-curves after LS. Similar trends were seen for the JV-curves measured under rear illumination.

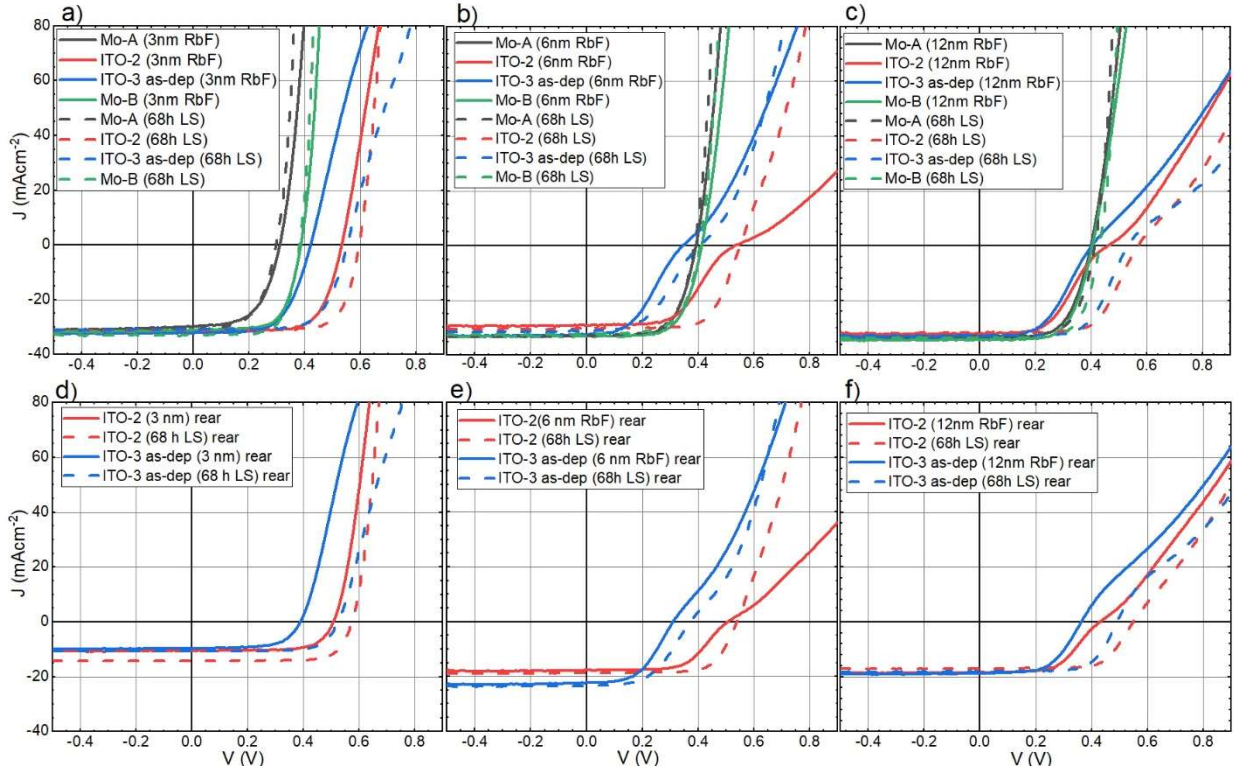


Figure 19 A study of RbF PDT on ITO-2 (red), as-deposited ITO-3 (blue), and two Mo reference pieces (black and green). Front-JV for the two ITO substrates and the two Mo references with a) 3 nm RbF, b) 6 nm RbF, c) 12 nm RbF, before (solid line) and after 68h LS (dashed line). Rear-JV for the two ITO substrates with d) 3 nm RbF, e) 6 nm RbF, f) 12 nm RbF, before and after 68h LS.

The difference in JV performance between the two ITO substrates can be explained by their different sheet resistivities and transmittances, see Table 1. ITO-2 has 7-8 times lower sheet resistivity, leading to a higher V_{OC} and FF, while the as-deposited ITO-3 has higher transmittance for wavelengths >900 nm, which can explain the improved J_{SC} under rear illumination. Interestingly, the ITO-2 devices improved more than the ITO-3 devices after LS with all three RbF thicknesses.

The two Mo samples in each batch were performing similarly, although the Mo-B sample is better than the Mo-A sample, irrespective of composition. It is therefore unlikely that it is the composition of the material, but rather the low temperature process, that is reducing the performance of the reference cells compared to the best cells on ITO. The exception is the 3 nm RbF batch, where the Mo-B sample is performing drastically better than Mo-A, and here it is safe to say that the Mo-A sample has a I/III ratio that is over-stoichiometric.

4.7. Some comments about stability

Comparing solar cell performance over all studies presented in this thesis, some of the most impressive ones were for the 550-650 nm ACIGS on ITO presented in chapter 4.2. It was therefore with disappointment that we discovered a decrease in performance of these devices when they were remeasured less than a year later. The degradation was mainly seen for the devices on ITO and affected V_{OC} and FF, see Figure 20 where JV-curves for a cell on Mo and on ITO are compared.

Figure 24 and Figure 25 in the appendix show the performance spread over the samples at the first measurement and the later measurement.

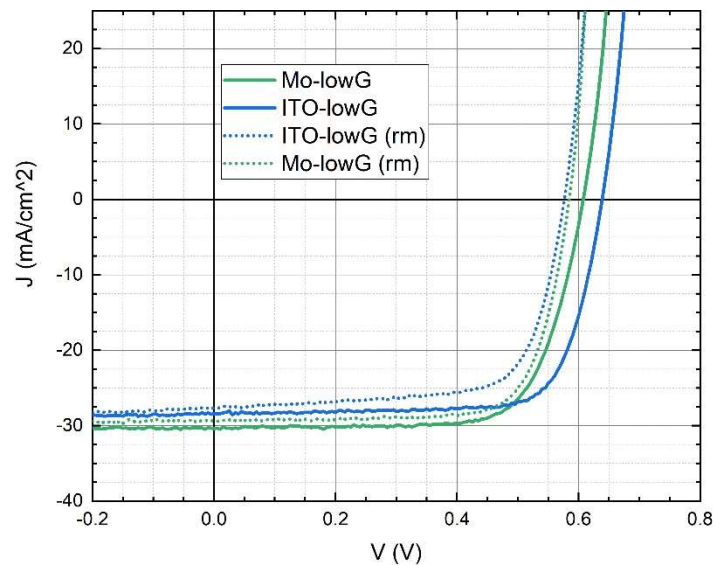


Figure 20 JV-curves for the best performing cell of sample Mo-lowG (green) and ITO-lowG (blue), as measured directly after device fabrication (solid lines), and re-measured (dotted lines) nine months later.

No further treatment or testing of the devices has as of yet been conducted, but the nature of the decaying performance is most puzzling, and will be the subject of further investigations. The fact that the degradation is more pronounced for the devices on ITO indicates some instability of the substrate, which may or may not be reversible.

5. Summary

The licentiate thesis has outlined some important properties of the ACIGS solar cell process and presented results showing what happens when we switch to a transparent back contact, ITO in our case. A new ACIGS process was established for ITO as a back contact, with a maximum deposition temperature of 450°C and a lower NaF precursor thickness. This process led to cell performances that superseded those of reference cells made on Mo back contacts, indicating that in some cases ITO can create a better back contact than Mo.

GaO_x was identified at the ITO/ACIGS interface, which previous research has shown having a detrimental effect on cell performance, but in our case its effect is believed to be beneficial. With the optimised ACIGS process, it is believed that the GaO_x layer was thin enough that it did not create a barrier for holes, but rather passivated the back surface together with the Ga-grading. It could be confirmed that GaO_x layer is catalysed by the NaF amount and the temperature, and not the Ga-concentration.

The conclusion of the conducted Ga-grading study was that the increase in GGI towards the back contact increases rear surface passivation. This passivation improves current collection, with observed gains in J_{SC} and FF, and decreases non-radiative recombination.

The importance of alkali treatment was seen in the experiments with NaF and RbF. When no NaF was provided to the ACIGS on ITO back contacts, the performance was deteriorating, but too much NaF combined with a high deposition temperature was also detrimental for performance. An optimum was found at 6 nm NaF precursor layer. An optimised amount of RbF for the new ACIGS process could not be determined within the scope of this thesis, but the best performance overall was achieved with 6 nm RbF PDT after 72 h of LS.

Finally, there is a concern of instability of the ITO substrates or the ITO/ACIGS interface, since deterioration of V_{OC} and FF was observed (mainly for cells on ITO) after some time in dark storage.

6. Outlook

Several research groups work on improving the back contact of ultrathin (≤ 500 nm) CIGS and introducing passivating or light-management structures. In a previous work with ACIGS absorbers fabricated at Uppsala, gold was used at the back contact to increase the internal reflectance. Au stripes were printed on top of Mo, since Mo is a poor reflector this addition of high-reflective metal was predicted to increase the current of the solar cell. To keep the Au from diffusing into the ACIGS during deposition, the metal was encapsulated in Al_2O_3 , which would also act as passivation of the rear contact. It was found that at standard deposition temperature ($550^\circ C$) the integrity of the Au metal structures and the dielectric were compromised, leading to the need to lower the deposition temperature to $450^\circ C$. With the lower deposition temperature, the high-reflective structures improved the J_{SC} and V_{OC} of the cells compared to those made on Mo references [36].

There are several reasons why the method of high-reflective back structures with dielectrics could be interesting to further test on ITO back contacts. Cells on ITO, having low internal reflectance, could with the addition of reflectors achieve higher J_{SC} , and the addition of the dielectric could provide further passivation of the back contact. Since the ITO process already works best at $450^\circ C$, the architecture used in [36] should be stable. The question is how much the cells would gain from the internal reflectance boost as opposed to being more transparent. Another question to consider is if the absorber material is truly of high quality at $450^\circ C$, or if there needs to be further process optimisation to avoid losses due to material defects.

To summarise, further studies that are of interest for the PhD thesis include:

- *The degradation of ACIGS cells on ITO during dark storage:*
What is causing the degradation?
Is the previously observed effect of V_{OC} loss reversible with LS or annealing?
What role do the light and heavy alkali play (i.e., is there movement of alkali)?
- *Improvement of the light-absorption in thin ACIGS:*
Can the ITO back contact be optimised for transparency by including metal grids at the back?
What light-management structures are compatible with the ACIGS process?

Should we move away from ITO to other TCOs with less parasitic absorption, but which are equally conductive, and thermally and chemically stable?

- *The role of the bifacial ACIGS in a tandem device:*

Can we grow perovskites directly on the standard ACIGS cell stack or do we need to change any layers?

Can a 2T ACIGS-only tandem be manufactured or will it have to be a 4T structure?

7. Acknowledgement

This thesis work would not have been possible without my wonderful supervisor, Marika Edoff. Thank you for your support, enthusiasm, and for teaching me how to become a better researcher. Thank you also to my co-supervisor, Tobias Törndahl, the collaborating partners of Hi-BITS, and the staff at MyFab Ångström, for your important roles in my work. And last, but not least, my heartfelt gratitude goes out to everyone at the Solar Cell Division in Uppsala for the welcoming environment, the engaging discussions and your support.

8. References

- [1] K. Calvin *et al.*, “IPCC, 2023: Climate Change 2023: Synthesis Report. Contribution of Working Groups I, II and III to the Sixth Assessment Report of the Intergovernmental Panel on Climate Change [Core Writing Team, H. Lee and J. Romero (eds.)]. IPCC, Geneva, Switzerland.” Intergovernmental Panel on Climate Change (IPCC), July 2023. doi: 10.59327/IPCC/AR6-9789291691647.
- [2] Y. Abdelilah *et al.*, “Renewables 2023 Analysis and forecast to 2028,” International Energy Agency, France, Jan. 2024. [Online]. Available: <https://www.iea.org/reports/renewables-2023>
- [3] M. Victoria *et al.*, “Solar photovoltaics is ready to power a sustainable future,” *Joule*, vol. 5, no. 5, pp. 1041–1056, May 2021, doi: 10.1016/j.joule.2021.03.005.
- [4] J. D. Bergesen, G. A. Heath, T. Gibon, and S. Suh, “Thin-Film Photovoltaic Power Generation Offers Decreasing Greenhouse Gas Emissions and Increasing Environmental Co-benefits in the Long Term,” *Environ. Sci. Technol.*, vol. 48, no. 16, pp. 9834–9843, Aug. 2014, doi: 10.1021/es405539z.
- [5] S. Philipps and W. Warmuth, “Photovoltaics report,” Fraunhofer Institute for Solar Energy Systems, ISE, May 2025. Accessed: Aug. 06, 2025. [Online]. Available: www.ise.fraunhofer.de
- [6] A. Maalouf, T. Okoroafor, Z. Jehl, V. Babu, and S. Resalati, “A comprehensive review on life cycle assessment of commercial and emerging thin-film solar cell systems,” *Renewable and Sustainable Energy Reviews*, vol. 186, p. 113652, Oct. 2023, doi: 10.1016/j.rser.2023.113652.
- [7] W. Shockley and H. J. Queisser, “Detailed Balance Limit of Efficiency of p-n Junction Solar Cells,” *J. Appl. Phys.*, vol. 32, no. 3, pp. 510–519, Mar. 1961, doi: 10.1063/1.1736034.
- [8] A. D. Vos, “Detailed balance limit of the efficiency of tandem solar cells,” *J. Phys. D: Appl. Phys.*, vol. 13, no. 5, p. 839, May 1980, doi: 10.1088/0022-3727/13/5/018.
- [9] B. Ehrler, E. Alarcón-Lladó, S. W. Tabernig, T. Veeken, E. C. Garnett, and A. Polman, “Photovoltaics Reaching for the Shockley–Queisser Limit,” *ACS Energy Lett.*, vol. 5, no. 9, pp. 3029–3033, Sept. 2020, doi: 10.1021/acsendergylett.0c01790.
- [10] S. S. Hegedus and A. Luque, *Knovel - Handbook of Photovoltaic Science and Engineering (2nd Edition)*, 2nd ed. John Wiley and Sons, 2011. Accessed: Apr. 17, 2024. [Online]. Available: <https://app.knovel.com/kn/resources/kpHPSEE002/toc>
- [11] M. Edoff and T. Jarmar, “High Voc in (Cu,Ag)(In,Ga)Se₂ Solar Cells,” *IEEE Journal of photovoltaics*, vol. 7, no. 6, Nov. 2017.
- [12] L. Chen, J. Lee, and W. N. Shafarman, “The Comparison of (Ag,Cu)(In,Ga)Se₂ and Cu(In,Ga)Se₂ Thin Films Deposited by Three-Stage Coevaporation,” *IEEE Journal of Photovoltaics*, vol. 4, no. 1, pp. 447–451, Jan. 2014, doi: 10.1109/JPHOTOV.2013.2280471.
- [13] J. Keller *et al.*, “High-concentration silver alloying and steep back-contact gallium grading enabling copper indium gallium selenide solar cell with 23.6% efficiency,” *Nat Energy*, pp. 1–12, Feb. 2024, doi: 10.1038/s41560-024-01472-3.
- [14] S. Siebentritt and T. P. Weiss, “Chalcopyrite solar cells —state-of-the-art and options for improvement,” *Sci. China Phys. Mech. Astron.*, vol. 66, no. 1, p. 217301, Dec. 2022, doi: 10.1007/s11433-022-2001-4.
- [15] S. Y. Chae, S. J. Park, O.-S. Joo, Y. Jun, B. K. Min, and Y. J. Hwang, “Highly stable tandem solar cell monolithically integrating dye-sensitized and CIGS solar cells,” *Sci Rep*, vol. 6, no. 1, Art. no. 1, Aug. 2016, doi: 10.1038/srep30868.
- [16] R. Kopecek and J. Libal, “Bifacial Photovoltaics 2021: Status, Opportunities and Challenges,” *Energies*, vol. 14, no. 8, p. 2076, Jan. 2021, doi: 10.3390/en14082076.
- [17] S.-C. Yang *et al.*, “Efficiency boost of bifacial Cu(In,Ga)Se₂ thin-film solar cells for flexible and tandem applications with silver-assisted low-temperature process,” *Nat Energy*, vol. 8, no. 1, Art. no. 1, Jan. 2023, doi: 10.1038/s41560-022-01157-9.

- [18] A. Ali *et al.*, “Highly Efficient Bifacial Narrow Bandgap Ag-CuInSe₂ Solar Cells on ITO,” *Advanced Energy Materials*, vol. n/a, no. n/a, p. 2500899, doi: 10.1002/aenm.202500899.
- [19] S.-C. Yang *et al.*, “Silver-Promoted High-Performance (Ag,Cu)(In,Ga)Se₂ Thin-Film Solar Cells Grown at Very Low Temperature,” *Solar RRL*, vol. 5, no. 5, p. 2100108, 2021, doi: 10.1002/solr.202100108.
- [20] P. Pearson, J. Keller, L. Stolt, O. Donzel-Gargand, and C. Platzer Björkman, “Ag-Dependent Behavior Threshold and Metastability in Wide-Gap (Ag,Cu)(In,Ga)Se₂ Solar Cells,” *Solar RRL*, vol. 8, no. 11, p. 2400220, 2024, doi: 10.1002/solr.202400220.
- [21] P. Pearson, J. Keller, L. Stolt, and C. Platzer Björkman, “Investigating the Role of Ag and Ga Content in the Stability of Wide-Gap (Ag,Cu)(In,Ga)Se₂ Thin-Film Solar Cells,” *physica status solidi (b)*, vol. 260, no. 7, p. 2300170, 2023, doi: 10.1002/pssb.202300170.
- [22] J. H. Boyle, B. E. McCandless, W. N. Shafarman, and R. W. Birkmire, “Structural and optical properties of (Ag,Cu)(In,Ga)Se₂ polycrystalline thin film alloys,” *J. Appl. Phys.*, vol. 115, no. 22, p. 223504, June 2014, doi: 10.1063/1.4880243.
- [23] K. Kiselman, J. Keller, P. Pearson, K. Sopiha, E. Wallin, and M. Edoff, “Light-Soaking Effects in High-Efficiency Cu(In,Ga)Se₂ and (Ag,Cu)(In,Ga)Se₂ Solar Cells,” *Progress in Photovoltaics: Research and Applications*, vol. 33, no. 7, pp. 735–746, 2025, doi: 10.1002/pip.3912.
- [24] S. Siebentritt, “Wide gap chalcopyrites: material properties and solar cells,” *Thin Solid Films*, vol. 403–404, pp. 1–8, Feb. 2002, doi: 10.1016/S0040-6090(01)01525-5.
- [25] W. N. Shafarman, R. Klenk, and B. E. McCandless, “Characterization of Cu(InGa)Se₂/sub 2/ solar cells with high Ga content,” in *Conference Record of the Twenty Fifth IEEE Photovoltaic Specialists Conference - 1996*, May 1996, pp. 763–768. doi: 10.1109/PVSC.1996.564240.
- [26] S. Siebentritt *et al.*, “Heavy Alkali Treatment of Cu(In,Ga)Se₂ Solar Cells: Surface versus Bulk Effects,” *Advanced Energy Materials*, vol. 10, no. 8, p. 1903752, 2020, doi: 10.1002/aenm.201903752.
- [27] M. A. Contreras, A. M. Gabor, A. L. Tennant, S. Asher, J. Tuttle, and R. Noufi, “Accelerated publication 16.4% total-area conversion efficiency thin-film polycrystalline MgF₂/ZnO/CdS/Cu(In,Ga)Se₂/Mo solar cell,” *Progress in Photovoltaics: Research and Applications*, vol. 2, no. 4, pp. 287–292, 1994, doi: 10.1002/pip.4670020404.
- [28] J. Ramanujam and U. P. Singh, “Copper indium gallium selenide based solar cells – a review,” *Energy Environ. Sci.*, vol. 10, no. 6, pp. 1306–1319, June 2017, doi: 10.1039/C7EE00826K.
- [29] T. Wada, N. Kohara, S. Nishiwaki, and T. Negami, “Characterization of the Cu(In,Ga)Se₂/Mo interface in CIGS solar cells,” *Thin Solid Films*, vol. 387, no. 1, pp. 118–122, May 2001, doi: 10.1016/S0040-6090(00)01846-0.
- [30] N. Naghavi *et al.*, “Buffer layers and transparent conducting oxides for chalcopyrite Cu(In,Ga)(S,Se)₂ based thin film photovoltaics: present status and current developments,” *Progress in Photovoltaics: Research and Applications*, vol. 18, no. 6, pp. 411–433, 2010, doi: 10.1002/pip.955.
- [31] W. Witte, S. Spiering, and D. Hariskos, “Substitution of the CdS buffer layer in CIGS thin-film solar cells,” *Vakuum in Forschung und Praxis*, vol. 26, no. 1, pp. 23–27, 2014, doi: 10.1002/vipr.201400546.
- [32] M. Edoff, S. Schleussner, E. Wallin, and O. Lundberg, “Technological and economical aspects on the influence of reduced Cu(In,Ga)Se₂ thickness and Ga grading for co-evaporated Cu(In,Ga)Se₂ modules,” *Thin Solid Films*, vol. 519, no. 21, pp. 7530–7533, Aug. 2011, doi: 10.1016/j.tsf.2011.01.369.
- [33] P. Reinhard *et al.*, “Flexible Cu(In,Ga)Se₂ solar cells with reduced absorber thickness,” *Progress in Photovoltaics: Research and Applications*, vol. 23, no. 3, pp. 281–289, 2015, doi: 10.1002/pip.2420.

- [34] O. Lundberg, M. Edoff, and L. Stolt, “The effect of Ga-grading in CIGS thin film solar cells,” *Thin Solid Films*, vol. 480–481, pp. 520–525, June 2005, doi: 10.1016/j.tsf.2004.11.080.
- [35] A. J. N. Oliveira, J. P. Teixeira, D. Ramos, P. A. Fernandes, and P. M. P. Salomé, “Exploiting the Optical Limits of Thin-Film Solar Cells: A Review on Light Management Strategies in Cu(In,Ga)Se₂,” *Advanced Photonics Research*, vol. 3, no. 6, p. 2100190, 2022, doi: 10.1002/adpr.202100190.
- [36] A. F. Violas *et al.*, “One-Step Lithography Nanostructured Au Encapsulation for Light Management in Ultrathin ACIGS Solar Cells,” *Solar RRL*, vol. n/a, no. n/a, p. 2400837, doi: 10.1002/solr.202400837.
- [37] C. Zhao *et al.*, “Advances in CIGS thin film solar cells with emphasis on the alkali element post-deposition treatment,” *Materials Reports: Energy*, vol. 3, no. 3, p. 100214, Aug. 2023, doi: 10.1016/j.matre.2023.100214.
- [38] P. Bras, C. Frisk, A. Tempez, E. Niemi, and C. Platzer-Björkman, “Ga-grading and Solar Cell Capacitance Simulation of an industrial Cu(In,Ga)Se₂ solar cell produced by an in-line vacuum, all-sputtering process,” *Thin Solid Films*, vol. 636, pp. 367–374, Aug. 2017, doi: 10.1016/j.tsf.2017.06.031.
- [39] S. Schleussner, U. Zimmermann, T. Wätjen, K. Leifer, and M. Edoff, “Effect of gallium grading in Cu(In,Ga)Se₂ solar-cell absorbers produced by multi-stage coevaporation,” *Solar Energy Materials and Solar Cells*, vol. 95, no. 2, pp. 721–726, Feb. 2011, doi: 10.1016/j.solmat.2010.10.011.
- [40] S. M. Schleussner, T. Törndahl, M. Linnarsson, U. Zimmermann, T. Wätjen, and M. Edoff, “Development of gallium gradients in three-stage Cu(In,Ga)Se₂ co-evaporation processes,” *Progress in Photovoltaics: Research and Applications*, vol. 20, no. 3, pp. 284–293, 2012, doi: 10.1002/pip.1134.
- [41] P. M. P. Salomé *et al.*, “A comparison between thin film solar cells made from co-evaporated CuIn_{1-x}Ga_xSe₂ using a one-stage process versus a three-stage process,” *Progress in Photovoltaics: Research and Applications*, vol. 23, no. 4, pp. 470–478, 2015, doi: 10.1002/pip.2453.
- [42] M. Morales-Masis, S. De Wolf, R. Woods-Robinson, J. W. Ager, and C. Ballif, “Transparent Electrodes for Efficient Optoelectronics,” *Advanced Electronic Materials*, vol. 3, no. 5, p. 1600529, 2017, doi: 10.1002/aelm.201600529.
- [43] J. Keller, L. Stolt, O. Donzel-Gargand, T. Kubart, and M. Edoff, “Wide-Gap Chalcopyrite Solar Cells with Indium Oxide-Based Transparent Back Contacts,” *Solar RRL*, vol. 6, no. 8, p. 2200401, 2022, doi: 10.1002/solr.202200401.
- [44] T. Nakada, Y. Hirabayashi, and T. Tokado, “Cu(In_{1-x}, Ga_x)Se₂-Based Thin Film Solar Cells Using Transparent Conducting Back Contacts,” *Jpn. J. Appl. Phys.*, vol. 41, no. 11A, p. L1209, Nov. 2002, doi: 10.1143/JJAP.41.L1209.
- [45] T. Hölscher *et al.*, “Effects of ITO based back contacts on Cu(In,Ga)Se₂ thin films, solar cells, and mini-modules relevant for semi-transparent building integrated photovoltaics,” *Solar Energy Materials and Solar Cells*, vol. 251, p. 112169, Mar. 2023, doi: 10.1016/j.solmat.2022.112169.
- [46] T. Nakada, Y. Hirabayashi, T. Tokado, D. Ohmori, and T. Mise, “Novel device structure for Cu(In,Ga)Se₂ thin film solar cells using transparent conducting oxide back and front contacts,” *Solar Energy*, vol. 77, no. 6, pp. 739–747, Dec. 2004, doi: 10.1016/j.solener.2004.08.010.
- [47] G. Dingemans and E. Kessels, “Status and prospects of Al₂O₃-based surface passivation schemes for silicon solar cells,” *J. Vac. Sci. Technol. A Vac. Surf. Films*, vol. 30, no. 4, 2012, doi: 10.1116/1.4728205.

- [48] B. Vermang *et al.*, “Introduction of Si PERC Rear Contacting Design to Boost Efficiency of Cu(In,Ga)Se₂ Solar Cells,” *IEEE Journal of Photovoltaics*, vol. 4, no. 6, pp. 1644–1649, Nov. 2014, doi: 10.1109/JPHOTOV.2014.2350696.
- [49] O. Lundberg, M. Bodegård, J. Malmström, and L. Stolt, “Influence of the Cu(In,Ga)Se₂ thickness and Ga grading on solar cell performance,” *Progress in Photovoltaics: Research and Applications*, vol. 11, no. 2, pp. 77–88, 2003, doi: 10.1002/pip.462.
- [50] B. Vermang, V. Fjällström, J. Pettersson, P. Salomé, and M. Edoff, “Development of rear surface passivated Cu(In,Ga)Se₂ thin film solar cells with nano-sized local rear point contacts,” *Solar Energy Materials and Solar Cells*, vol. 117, pp. 505–511, Oct. 2013, doi: 10.1016/j.solmat.2013.07.025.
- [51] P. M. P. Salomé *et al.*, “Incorporation of Na in Cu(In,Ga)Se₂ Thin-Film Solar Cells: A Statistical Comparison Between Na From Soda-Lime Glass and From a Precursor Layer of NaF,” *IEEE Journal of Photovoltaics*, vol. 4, no. 6, pp. 1659–1664, Nov. 2014, doi: 10.1109/JPHOTOV.2014.2357261.
- [52] M. Edoff, T. Törndahl, F. Larsson, O. Stolt, N. Shariati-Nilsson, and L. Stolt, “Post Deposition Treatments of (Ag,Cu)(In,Ga)Se₂ Thin Films for Solar Cells,” in *2019 IEEE 46th Photovoltaic Specialists Conference (PVSC)*, June 2019, pp. 0618–0621. doi: 10.1109/PVSC40753.2019.8981287.
- [53] A. Rockett *et al.*, “Na in selenized Cu(In,Ga)Se₂ on Na-containing and Na-free glasses: distribution, grain structure, and device performances,” *Thin Solid Films*, vol. 372, no. 1, pp. 212–217, Sept. 2000, doi: 10.1016/S0040-6090(00)01028-2.
- [54] L. Mansfield *et al.*, “Sodium-doped molybdenum targets for controllable sodium incorporation in CIGS solar cells,” *Conference Record of the IEEE Photovoltaic Specialists Conference*, pp. 003636–003641, June 2011, doi: 10.1109/PVSC.2011.6185937.
- [55] S. Ishizuka, N. Taguchi, J. Nishinaga, Y. Kamikawa, and H. Shibata, “A comparative study of the effects of light and heavy alkali-halide postdeposition treatment on CuGaSe₂ and Cu(In,Ga)Se₂ thin-film solar cells,” *Solar Energy*, vol. 211, pp. 1092–1101, Nov. 2020, doi: 10.1016/j.solener.2020.10.048.
- [56] D. Adeleye *et al.*, “Wide-Bandgap Cu(In, Ga)S₂ Solar Cell: Mitigation of Composition Segregation in High Ga Films for Better Efficiency,” *Small*, vol. 21, no. 8, p. 2405221, 2025, doi: 10.1002/smll.202405221.
- [57] F. Pei *et al.*, “Perovskite/CIGS Tandem Solar Cells with over 1000 h Operational Stability through Interconnection Stress Relief,” *J. Am. Chem. Soc.*, Sept. 2025, doi: 10.1021/jacs.5c13264.
- [58] F. Pei *et al.*, “Inhibiting defect passivation failure in perovskite for perovskite/Cu(In,Ga)Se₂ monolithic tandem solar cells with certified efficiency 27.35%,” *Nat Energy*, vol. 10, no. 7, pp. 824–835, July 2025, doi: 10.1038/s41560-025-01761-5.
- [59] Martin A. Green, *Solar Cells - Operating Principles, Technology and System Applications*. The University of New South Wales, 1998.
- [60] Elizaveta Yakovleva *et al.*, “Back contact passivation with Ga-grading in narrow bandgap (Ag,Cu)(In,Ga)Se₂ bifacial solar cells on In₂O₃:Sn back contact,” Aug. 28, 2025.
- [61] I. Pelant and J. Valenta, *Luminescence Spectroscopy of Semiconductors*, 1st ed. Oxford: OUP Oxford, 2012. doi: 10.1093/acprof:oso/9780199588336.001.0001.
- [62] Douglas A. Skoog, F. James Holler, and Timothy A. Nieman, *Principles of Instrumental Analysis*, 5th ed., vol. 1998. USA: Saunders College Publishing.
- [63] N. W. Barnett *et al.*, *Glow Discharge Optical Emission Spectroscopy: A Practical Guide*. La Vergne, UNITED KINGDOM: Royal Society of Chemistry, The, 2003. Accessed: Oct. 23, 2025. [Online]. Available: <http://ebookcentral.proquest.com/lib/uu/detail.action?docID=1185581>

- [64] D. B. Williams and C. B. Carter, *Transmission Electron Microscopy: A Textbook for Materials Science*. New York, NY, UNITED STATES: Springer, 1996. Accessed: Oct. 23, 2025. [Online]. Available: <http://ebookcentral.proquest.com/lib/uu/detail.action?docID=3084962>

Appendix

9. Theory of characterization methods

9.1. Electrical and optical characterization

9.1.1. Current-voltage

Measurement of solar cell performance involves measuring the power output of the solar cell under Standard test conditions (STC). The standard performance measurement involves a current-voltage (IV) sweep while the solar cell is illuminated by a light-source with a spectrum closely matching the AM1.5 spectrum at an irradiation power of 1000 W/m^2 while maintaining a cell temperature of 25°C . Alternatively, the solar cell is kept in the dark for dark-IV measurement. Four-point contacting probes are employed to keep voltage and current leads to the cell separate. This removes effects of series resistances in the probes as well as contact resistances [59]. The result can be presented as an IV-curve or a current-density (JV) curve (see Figure 2), from which the performance characteristics J_{SC} , V_{OC} , FF, J_{mp} , V_{mp} , and efficiency can be extracted.

9.1.2. External quantum efficiency

External quantum efficiency (EQE) measurements measure the collected electrons per incoming photons over a range of wavelengths. The EQE-value is useful to see collection losses in the solar cell, and can be integrated over the wavelengths to give the short-circuit current:

$$J_{SC} = q \int_0^\infty EQE(\lambda)\phi(\lambda)d\lambda, \quad (7)$$

where ϕ is the photon flux corresponding to the sunlight at STC at each wavelength and λ is the wavelength [59]. In practice, the measurement is carried out by illuminating a small area of the solar cell in a wavelength interval, with an upper limit around the bandgap. The incoming light is calibrated using one or more solar cells (to cover the wavelength span) with pre-calibrated characteristics.

9.1.3. Capacitance-voltage

The pn-junction can be modelled as a parallel-plate capacitor, with plates of area A (cell area) separated by the depletion width, W . This measurement is facilitated if one side of the pn-junction is more heavily doped than the other, and if the depletion region is found on only the lower doped side.

The capacitance of the depletion region is given by,

$$C = \frac{\epsilon A}{W}, \quad (8)$$

where ϵ is the electrical permittivity of the materials in the junction region.

In the case of a CIGS solar cell with a CdS buffer layer, a high resistance ZnO and a doped ZnO an assumption often made, is that the depleted region, W , is found solely in the CIGS layer, then

$$\frac{C}{A} = \left[\frac{q\epsilon N}{2(\psi_0 - V_a)} \right]^{1/2}, \quad (9)$$

where N is the doping density N_A (acceptor dopant density), ψ_0 is the built-in potential of the pn-junction, and V_a is the applied voltage.

By applying reverse bias to the solar cell and measuring C , then plotting $1/C^2$ as a function of applied voltage, the minority carrier doping N can be found.

By varying the reverse bias to the solar cell, applying an AC current and measuring the capacitance, C , then by plotting $1/C^2$ as a function of applied voltage, the depletion region width at zero volt applied voltage, and minority carrier doping N_a can be calculated [59]. Only the part of the CIGS layer that can be depleted by the reverse bias can be characterized, but it is a useful measurement to compare effects of various compositional changes of the CIGS absorber as well as effects of e.g. light soaking.

9.1.4. Photoluminescence

Photoluminescence (PL) is excitation brought about by absorption of photons, which in turn can lead to emission of photons (luminescence). A suitable excitation wavelength, which will excite the material of interest (excitation energy should be higher than the bandgap), is selected to illuminate the sample. Lasers are commonly used as excitation sources. Emitted luminescence is collected, channelled into a detector, and turned into a plot of luminescence intensity as a function of wavelength, also called emission spectra.

The excited, free electron transitions after some relaxation time to the ground state. The transition can happen radiatively (emission of light) or non-radiatively (emission of vibrations to the crystal lattice). The ratio of the radiative transition rate to the total transition rate is defined as the *quantum yield*, and says something about how luminescent a material is. Channels for radiative transitions include band-to-band recombinations of electrons and holes, recombinations of free electrons (holes) with a shallow acceptor (donor) state, also called an impurity as it introduces bound states (or traps) within the bandgap, and recombinations between donor and acceptor states. Non-radiative transitions are related to energy-loss mechanisms such as heat transfer, Auger recombination, creation of defects in the lattice, and photochemical changes of the material.

The PL spectrum of band-to-band recombinations of free electrons and holes follows the Maxwell-Boltzmann distribution, with the lower energy emission determined by the bandgap, E_g , and the higher energy tail determined by temperature. Transitions between bands and impurity levels have lower emission than direct band-to-band recombinations. For example, an electron that has transitioned to a shallow acceptor state will usually go on to recombine non-radiatively with a hole close to the VBM, thus only part of the energy from the excited state will be emitted radiatively. Transitions to donor and acceptor states are usually only visible at low temperature PL, because

the states are already ionised at room temperature. If the studied material is not pure, several peaks may appear in the PL spectrum.

General source: “Luminescence Spectroscopy of Semiconductors” by Ivan Pelant and Jan Valenta [61].

It has already been mentioned that V_{OC} losses are connected to carrier recombination. It is therefore especially interesting to study PL of a cell to understand the V_{OC} performance. PL is also useful to extract the Urbach energy [14].

9.2. Material characterization

9.2.1. X-ray fluorescence spectroscopy

X-ray fluorescence (XRF) spectroscopy is a non-destructive elemental analysis technique, commonly used for identification of elements heavier than oxygen, as well as quantitative analysis of elemental composition. The technique uses an X-ray beam to irradiate the sample and measures characteristic radiation emitted from the excited elements in the analysed material.

The principle of XRF is excitation of inner shell atomic electrons in the atoms, which upon relaxation will emit characteristic X-rays. The excited electron will leave an empty electronic state in an inner shell (K-shell or L-shell) of the atom. When the electron relaxes by transitioning from the higher electronic states it emits photons of energies which are usually slightly lower than the energy needed to excite the electron. Most of the emitted photons fall into two series: the K series for transitions down to the K-shell, and the L series for transitions to the L shell. The energy transitions, and photon emissions, are characteristic of each element, resulting in intensity peaks at the characteristic wavelengths of the K series and L series that can be used to identify the element.

The XRF spectroscopy technique is not sensitive to physical or chemical state of the elements, such as if it is a pure metal or an oxide.

For quantitative analysis of a sample, the area under the peak intensities is used to determine the concentration of each element in the sample. There are however effects that can make this analysis incorrect. Matrix effects are caused by the fact that the excitation of atoms happens in the bulk of the sample as well as on the surface. When the emitted X-rays travel through the bulk material they are attenuated through scattering and absorption to a degree which depends on the mass absorption coefficient, which is influenced by all elements of the sample. There can also be enhancement of certain emission lines through secondary emission. All these effects can be taken into account with calibration methods, such as comparing the line intensities of the sample to a known standard reference. This calibration is dependent on the assumption that the sample and the reference are close in composition and that all matrix effects are identical in both cases.

General source: “Principles of Instrumental analysis”, Chapter 12, by D. A. Skoog, F. J. Holler and T. A. Nieman [62, Ch. 12].

9.2.2. Mass spectrometry

Mass spectrometry (MS) or atomic MS is used for analysis of the atomic mass concentrations of a sample, and is also commonly used in vacuum analysis. The technique involves the following steps: atomization, ionization of the atoms, separation of the ions into bins according to their mass-to-charge ratio (m/z), and counting the incoming ions belonging to each bin. A number of different instruments exist that use the mass spectrometry method. Common for all MS instruments is the need for high vacuum to increase the mean free path of the ions travelling towards the transducer, which converts their impact into an electrical signal.

A common type of mass spectrometer is the quadrupole mass analyser, because it is compact and fast. The instrument consists of four rods mounted in parallel along the ions' path. The opposing rod pairs are connected, with one pair having a positive DC potential, and the other a negative DC potential. Variable radio-frequency (RF) AC potentials are applied to each pair of rods at a 180° difference in phase. The ions are accelerated into the space between the rods, and at the same time the DC and AC potentials of the rods are ramped up. The DC potentials between the negative and positive rod pairs act as a narrow-band filter for the ion mass, while the AC potential will alternate between focusing and dispersing the ion beam along the centre of the path between the rods. Together, the potentials are used to limit a range of m/z values that can pass between the rods with a stable trajectory towards the transducer. All ions with other m/z ratios will touch the rods and become annihilated. To perform the mass scan, the DC and AC potentials are increased from zero to a maximum value, while maintaining a constant ratio between them as this determines the resolution of the quadrupole.

General source: "Principles of Instrumental analysis", Chapter 11, by D. A. Skoog, F. J. Holler and T. A. Nieman [62, Ch. 11].

9.2.3. Glow discharge optical emission spectroscopy

Glow Discharge Optical Emission Spectroscopy (GDOES) is a spectroscopy technique used to analyse elemental composition and thickness of samples containing, among others, metals, semiconductor materials, and glass. The GDOES detector setup includes a glow discharge (GD) source, which generates a plasma from ionised argon (Ar^+) gas, optical spectrometer, a cooling system, and vacuum pump. The measurement is done by gradually sputtering through the sample, exciting the sputtered sample particles that emit photons, which are measured in the spectrometer to characterise the elements of the sample. The sample acts as a cathode and the GD source as the anode. The Ar plasma is formed by electrons from the cathode colliding with the Ar atoms when a DC voltage bias is applied between the cathode and anode. Since the sample effectively acts as a cathode it has to be conductive unless the setup allows for an alternating voltage regime. The plasma ionises some of the sample atoms, which together with the Ar^+ ions fly back towards the sample surface and sputter it to release more atoms.

Electrons excite the sputtered atoms in the plasma, making them emit characteristic photon emission when they de-excite. The spectrometer at the GD source records the intensities of all the elemental emissions. Adding all of them up, and taking into account the background, scattering, self-absorption, and other noise in the detector, should give the complete composition of the

sample. For each element and sputtering time interval, the signal has to be calibrated to take into account the relative sputtering rate and emission yield of each element. Integrating over the sputtering time yields the sputtered mass of each element. An XRF measurement can then give the ratio between the different elements of the composition.

General source: "Glow Discharge Optical Emission Spectroscopy : A Practical Guide" by Richard Payling, Thomas Nelis and Neil W. Barnett [63].

9.3. Electron microscopy

Electron microscopy is used to study material under much higher magnification than what is possible in an optical microscope. Instead of a focused beam of light, electron microscopes use magnetic coils to focus an electron beam on the sample. Transmission electron microscopy (TEM) and Scanning transmission electron microscopy (STEM) are two common techniques used to study bulk material properties. The difference between the two techniques is that TEM has a parallel beam and one detector, while STEM has a focused beam and multiple detectors for different contrasts. Modern TEM and STEM instruments can have a resolution down to 20-1 pm, which is governed by the wavelength, and thus energy, of the electron beam. Scanning electron microscopy (SEM) is also a common technique which is used to study surfaces, because unlike TEM and STEM the electron beam does not penetrate through the sample. The challenges with all these techniques come from the interactions of the electron beam with the material of the sample, which can lead to sample damage and difficulty interpreting the resulting images.

Energy Dispersive X-ray Spectroscopy (EDS or EDX) is a spectroscopy technique that can be used in combination with STEM or TEM. A STEM or TEM image is taken of the sample, an area of interest is found and the EDS maps the atomic concentrations in that area. The EDS detector is placed above the sample and collects atomic information based on the characteristic X-rays emitted from the sample when the atoms are excited by the incoming electron beam. It is important to note that EDS is not very sensitive to light elements, and has a lower spatial resolution than STEM/TEM.

General source: "Transmission Electron Microscopy: A Textbook for Materials Science" by William and Carter [64].

10. ACIGS deposition recipes

10.1. Cell processing post absorber deposition

CdS deposition was performed with chemical bath deposition (CBD). A solution of 1.1 M ammonium hydroxide (NH_4OH), 3 mM cadmium acetate ($\text{Cd}(\text{O}_2\text{CCH}_3)_2(\text{H}_2\text{O})_2$), and 100 mM thiourea ($(\text{NH}_2)_2\text{CS}$) was mixed before submersion of the ACIGS samples. The solution with the ACIGS samples was then heated in a water bath at 60°C . A CBD process time of 8.25 minutes resulted in ~ 50 nm CdS, while a process time of 5.5 minutes resulted in a ~ 30 nm layer of CdS. The thinner layer was only used when the ACIGS had been treated with RbF PDT.

AZO and intrinsic ZnO (i-ZnO) were deposited in the von Ardenne sputter, model CS730. AZO was sputtered using radio-frequency (RF) magnetron sputtering. First, a layer of undoped ZnO was deposited by sputtering the AZO target at high oxygen content (3.0 sccm) for 50 s. The high oxygen content avoids doping the ZnO, and was convenient since no undoped ZnO target was installed in the sputter. Secondly, a layer of AZO was sputtered at low oxygen content (~ 0.3 - 0.4 sccm) for 400 s. The total window layer was approximately 200 nm thick and had sheet resistances in the range of 35-50 Ohm/Sq .

10.2. Cell definition with photolithography

The detailed photolithography steps for cell definition, used for making the cells in this thesis, were as follows:

1. Coating: $2,5 \times 2,5$ cm^2 samples with ACIGS, CdS and AZO window layer were spin-coated with AZ10XT photoresist. After being covered with a symmetric layer of the resist, the samples were rotated for 30 s at 6000 rpm with a 5s ramp-up and ramp-down time.
2. Soft bake: the resist was heated on a hot plate at 110°C for 120s.
3. Patterning: the resist was exposed under UV-light, 4 times for 30 s with 45 s waiting time.
4. Development: pattern was developed in AZ 400K developer (1:4 with water), 3 min per sample, rinsed in water and dried.
5. Hard bake: heating on a hot plate at 120°C for 120s.
6. Etching: cells were etched in 1 M hydrochloric acid (HCl) for 1 min, alternatively in 10% acetic acid for 3 min.
7. Cleaning: the remaining photoresist was removed in acetone (15 min) and the samples were rinsed with isopropanol afterwards. The glass side of bifacial samples was carefully cleaned with 1 M HCl of any remaining CdS.

11. Optimisation of ACIGS process for ITO: additional figures

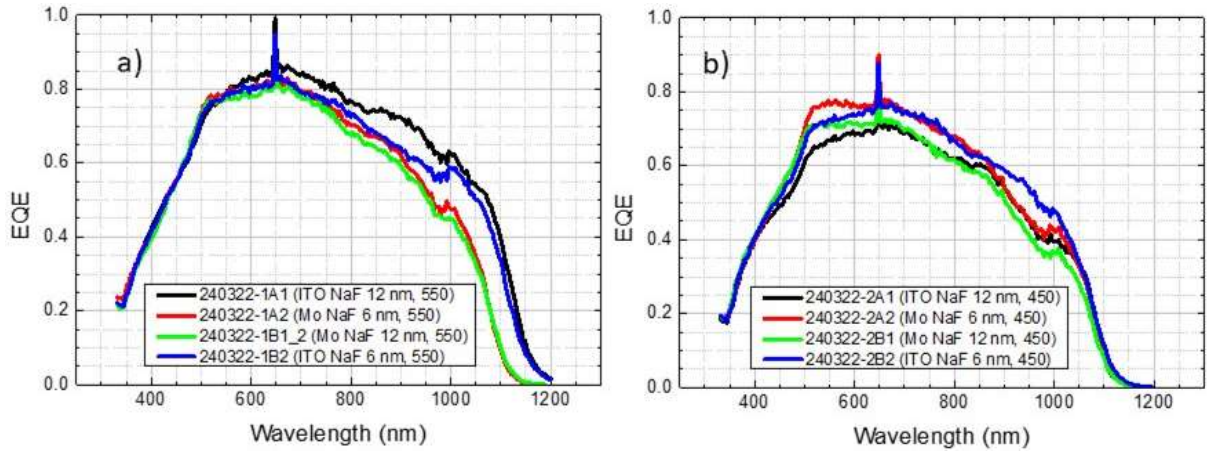


Figure 21 EQE of the best performing cells of the process optimisation study: ACIGS deposited at 550°C and 450°C on ITO and Mo with 12 nm and 6 nm NaF. The figure on the left (a) presents the run at 550°C, and the figure on the right (b) presents the run at 450°C. The one-point peak in EQE at the wavelength 650 nm is caused by a discrepancy in the calibration file. For the deposition run at 550°C the cells on ITO (black and blue) have a decreased bandgap, increasing their absorption.

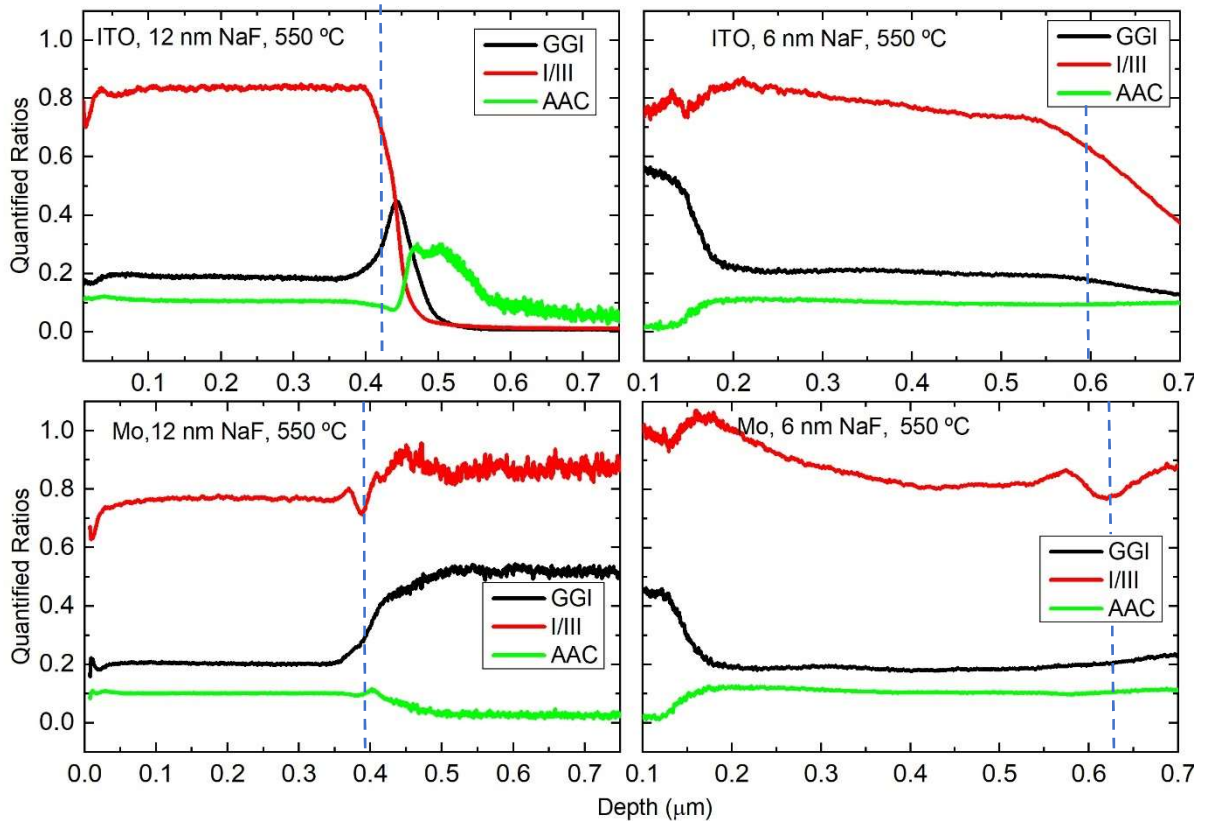


Figure 22 Quantified ratios of GGI, I/III, and AAC from GODES measurements of ~500 nm ACIGS deposited at 550°C on ITO with 12 nm NaF (top-left), ITO with 6 nm NaF (top-right), Mo with 12 nm NaF (bottom-left), and Mo with 6 nm NaF (bottom-right). The blue, vertical line indicates approximately where the interface between the absorber and the back contact is.

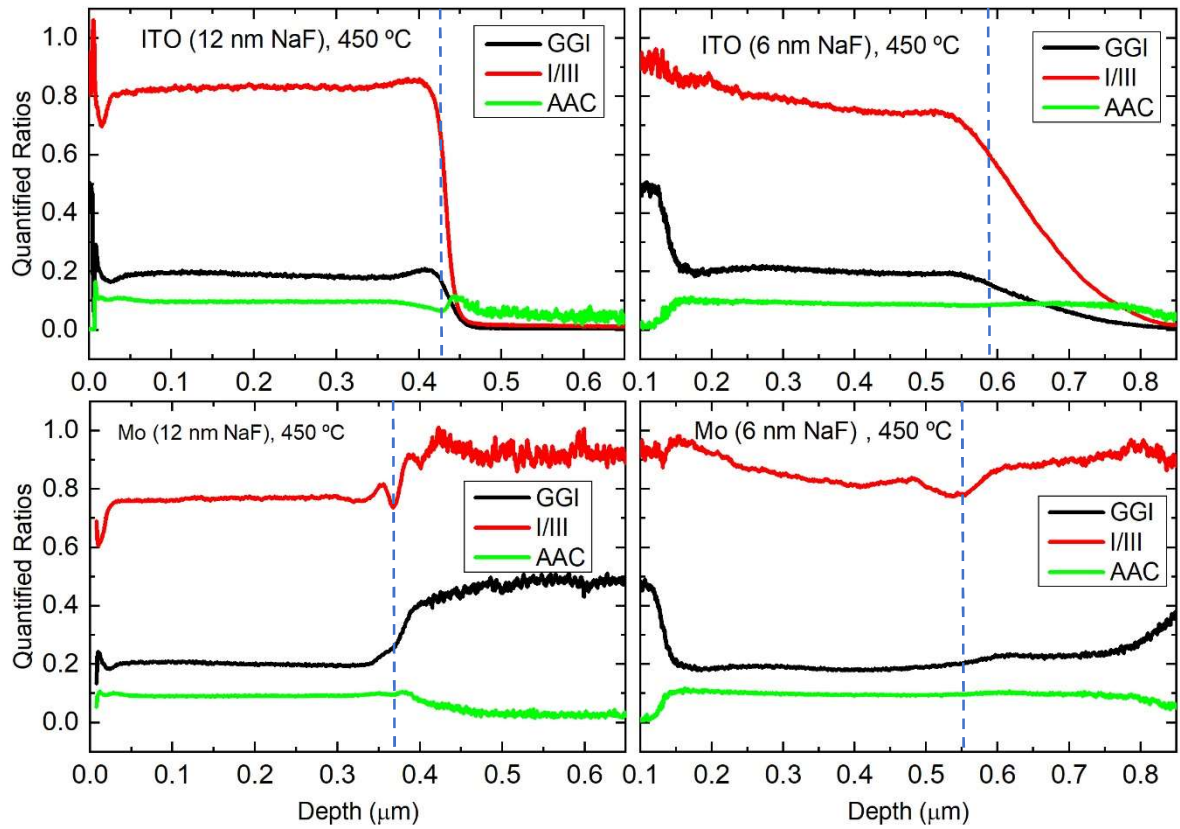


Figure 23 Quantified ratios of GGI, I/III, and AAC from GODES measurements of ~500 nm ACIGS deposited at 450°C on ITO with 12 nm NaF (top-left), ITO with 6 nm NaF (top-right), Mo with 12 nm NaF (bottom-left), and Mo with 6 nm NaF (bottom-right). The blue, vertical line indicates approximately where the interface between the absorber and the back contact is.

12. Deterioration of performance after dark storage

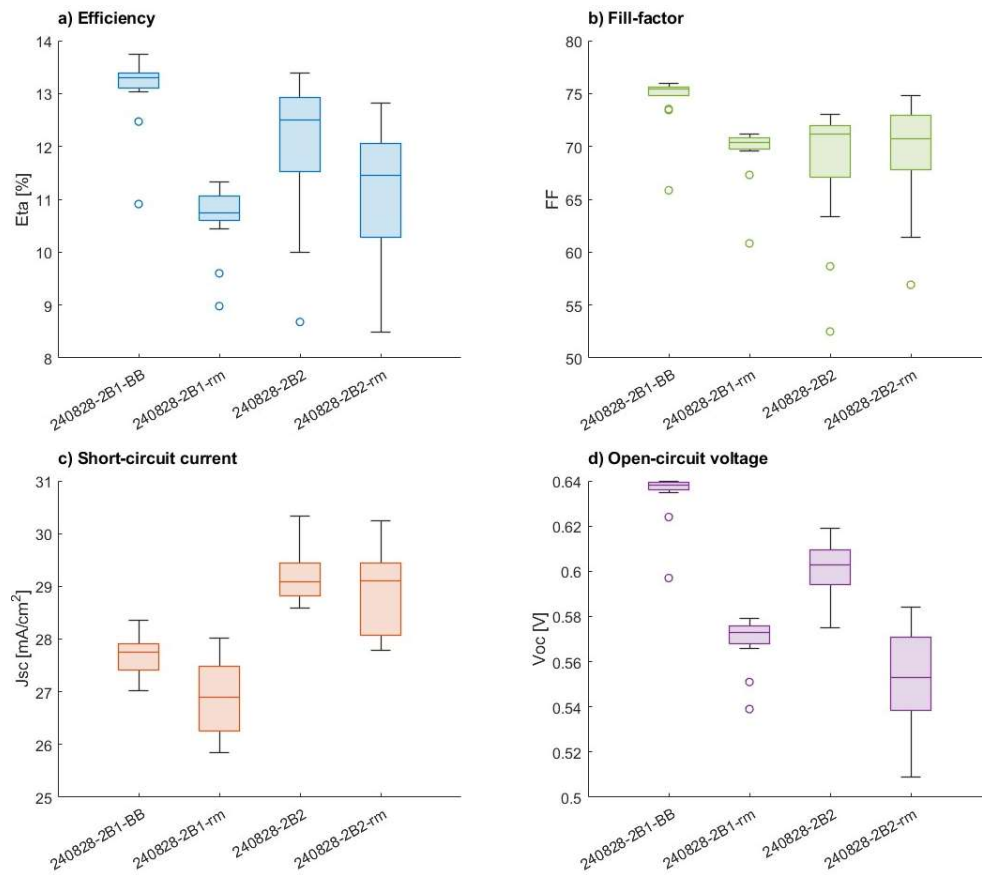


Figure 24 Boxplots with a) efficiency, b) FF, c) J_{sc} , and d) V_{oc} , for two samples from the 550 nm ACIGS with low Ga-grading (ITO-lowG and Mo-lowG), first measured in September 2024, and later re-measured (rm) in late May 2025 in the same IV-setup. The sample labelled 240828-2B1 is on ITO substrate, and the sample labelled 240828-2B2 is on a Mo substrate. The suffix -rm in the label indicates the re-measured values.

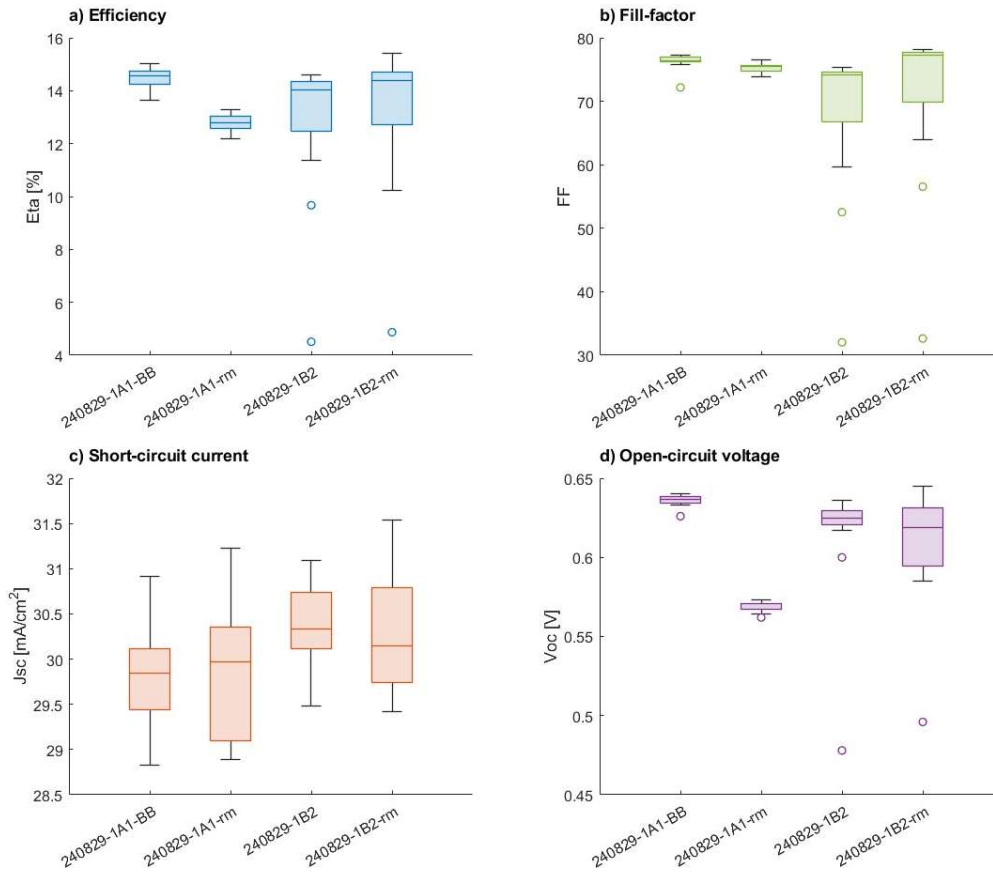


Figure 25 Boxplots with a) efficiency, b) FF, c) Jsc, and d) Voc, for two samples from the 650 nm ACIGS with high Ga-grading (ITO-highG and Mo-highG), first measured in September 2024, and later re-measured (rm) in late May 2025 in the same IV-setup. The sample labelled 240829-1A1 is on an ITO substrate and 240829-1B2 is on a Mo substrate. The suffix -rm in the label indicates the re-measured values.

13. Manuscript